

Error scaling of large-eddy simulation in the outer region of wall-bounded turbulence

A. Lozano-Durán¹ and H. J. Bae^{1,2}

¹*Center for Turbulence Research, Stanford University*

²*Institute for Computation and Mathematical Engineering, Stanford University*

(Dated: June 25, 2019)

We study the error scaling properties of implicitly-filtered large-eddy simulation (LES) in the outer region of wall-bounded turbulence at moderately high Reynolds numbers and for different subgrid-scale (SGS) models. In order to avoid the additional complexity of wall-modeling, we perform LES of turbulent channel flows where the wall boundary condition is replaced by a Neumann condition supplying the exact mean wall stress. The statistics under consideration are the mean velocity profile, turbulence intensities, and kinetic energy spectra. The errors for these quantities follow $(\Delta/L)^\alpha Re_\tau^\gamma$, where Δ is the characteristic grid resolution, Re_τ is the friction Reynolds number, and L is the relevant length-scale to refer Δ . It is shown that Δ can be expressed as the L_2 -norm of the grid vector, and L is well represented by the ratio of the friction velocity and mean shear. The exponent α is estimated from theoretical arguments for each statistical quantity of interest and is shown to roughly match the values computed by numerical simulations. For the mean profile and kinetic energy spectra, $\alpha \approx 1$, whereas the turbulence intensities converge at a slower rate $\alpha < 1$. The exponent γ is approximately 0, and the LES solution is independent of the Reynolds number. Further analysis reveals that the turbulence intensities and spectra resemble their filtered counterparts computed from direct numerical simulation (DNS) data, but the mechanism responsible for this similitude is related to the balance of the input power and dissipation rather than to filtering. The expected behavior of the turbulence intensities at high Reynolds numbers is also derived and shown to agree with the classic log-layer profiles for grid resolutions lying within the inertial range.

I. INTRODUCTION

Most turbulent flows cannot be calculated by DNS of the Navier-Stokes equations because the range of scales of motions is so large that the computational cost becomes prohibitive. In LES, only the large eddies are resolved, and the effect of the small scales on the larger scales is modeled through an SGS model. The approach enables a reduction of the computational cost by several orders of magnitude while still capturing the statistical quantities of interest. However, the solutions provided by most LES approaches are grid-dependent, and multiple computations are required in order to faithfully assess the quality of the LES results. This brings the fundamental question of what is the expected LES error as a function of Reynolds number and grid resolution. The necessity of assessing the impact of grid resolution on both the accuracy and convergence properties of SGS models and flow statistics has been highlighted in the NASA Vision 2030 [1] as a pacing item for the computational fluid mechanics community. The issue was also remarked by Pope [2] as a central problem concerning the foundations of LES. Therefore, LES must be framed in the context of a convergence study, and the associated grid requirements for different flow configurations must be determined for LES to be deemed as a cost-saving approach when compared with DNS. In the present work, we analyze the LES error scaling of the mean velocity profile, turbulence intensities, and energy spectra in the outer region of wall-bounded flows without the influence of the wall.

The equations for LES are formally derived by applying a low-pass filter to the Navier-Stokes equations [3]. The common procedure is then to solve these filtered equations together with a model for the SGS stresses, but no explicit filter form is usually specified. Instead, the discrete differentiation operators and limited grid resolution used to compute the LES solution are assumed to act as an effective implicit filter. The approach, usually referred to as implicitly-filtered LES, yields a velocity field that is considered representative of the actual filtered velocity with filter size proportional to the grid resolution. This lack of explicit filtering is responsible for the aforementioned intimate relation between the grid resolution and the LES equations. Grid convergence is only guaranteed in the limit of DNS-like resolution, and the LES predictions may be sensitive in an intricate manner to the grid size above such limit. This is a distinctive feature of implicitly-filtered LES which entails important difficulties for evaluating the quality of the solutions.

First works aiming to assess the accuracy of SGS models include the pioneering investigation by Clark et al. [4], who established the numerical study of decaying isotropic turbulence as a reference benchmark, although the grid resolutions and Reynolds numbers tested were highly constrained by the computational resources of the time. Since then, common benchmarks for LES have broadened to include simple hydrodynamic cases such as forced or decaying isotropic turbulence [5], rotating homogeneous turbulence [6], spatial or temporal mixing layers [7, 8] and plane turbulent channel flow [9, 10, 11], among others. See [12] for an overview of cases for LES validation.

Recent developments in modeling and numerical error quantification in isotropic turbulence by Meyers et al. [13]

showed that the partial cancellation of both sources can lead to coincidentally accurate results. Along the same line, Meyers et al. [14] studied the combined effect of discretization and model errors, and a further series of works resulted in the error-landscape-methodology framework reviewed by Meyers [15], where it is stressed that the determination of the quality of LES based on one metric alone may provide misleading results. The performance of SGS models in the presence of walls has been found to be even more erratic. Meyers and Sagaut [16] presented the grid convergence behavior of channel flow LES at resolutions typically encountered in SGS model testing. They observed a non-monotonic convergence of the skin friction and turbulence intensities with grid-refinements, suggesting that the robustness of SGS models should be tested for a range of Reynolds numbers and resolutions in order to avoid incidental coincidences with DNS results. At much higher Reynolds numbers, Sullivan and Patton [17] examined the numerical convergence of LES in time-dependent weakly sheared planetary boundary layers. They considered the convergence of the second-order statistics, energy spectra, and enthalpy statistics, and concluded that LES solutions are grid-independent provided that there is adequate separation between the energy-containing eddies and those near the filter cut-off scale. Stevens et al. [18] showed the ability of LES to reproduce accurately second and higher-order velocity moments for grid resolutions fine enough to resolve 99% of the LES kinetic energy. The convergence of SGS models in complex geometries has been explored in a lesser degree, but some noteworthy efforts are the pulsatile impinging jet in turbulent cross-flow by Toda et al. [19] and the full plane calculations using the NASA Common Research Model by Lehmkuhl et al. [20].

A central matter among the convergence studies above is the search for the most meaningful flow quantity to collapse the LES errors when the grid size, Reynolds number, and model parameters are systematically varied. Geurts and Fröhlich [21] characterized the simulation errors in terms of the subgrid-activity, defined as the relative subgrid-model dissipation rate with respect to the total dissipation rate. Klein [22] studied the accuracy of single-grid estimators for the unresolved turbulent kinetic energy to assess the quality of LES, and evaluated the sensitivity of the LES results on the modeling and numerical errors. Similarly, Freitag and Klein [23] presented a method to evaluate error contributions by assuming that the numerical and modeling errors scale like a power of the grid spacing and filter width, respectively. Other indices to estimate the quality of the LES solution are the fraction of the total turbulent kinetic energy in the resolved motions [2], the relative grid size with respect to Kolmogorov or Taylor scales, or the effective eddy viscosity compared to the molecular viscosity [24]. Alternative and more sophisticated metrics are still emerging, for instance, the Lyapunov exponent measurement proposed by Nastac et al. [25] for assessing the dynamic content and predictability of LES among others, but there is a lack of consensus regarding which should be the most meaningful metric to quantify errors in a general set-up, if any.

In the present work, we assess the error scaling of two SGS models based on the eddy viscosity assumption in the outer region of wall-bounded turbulence at moderately high Reynolds numbers. Our goal is to characterize the errors as a function of grid resolution and Reynolds number, and to find the physical length-scale dictating the relative size of the grid that is relevant for error quantification. For that purpose, we perform a theoretical estimation of the error scaling for the mean velocity profile, turbulence intensities, and kinetic energy spectra. Our results are corroborated by numerical simulation of LES turbulent channel flows using a wall model that acts as a surrogate of the near-wall dynamics by supplying the exact mean wall stress. It is important to remark that turbulent free shear flows such as mixing layers, jets, and wakes are also tenable candidates for studying shear-dominated flows away from the wall. However, their large scales are dynamically different to the large motions of turbulent boundary layer flows typically relevant for external aerodynamics, which is the focus of the present study.

The manuscript is organized as follows. In section II, we illustrate the necessity of wall models before SGS models in LES. We discuss the methodology and numerical setup to assess the convergence of SGS models in the outer-layer of wall-bounded turbulence in section III. The results for the errors in the mean velocity profile are presented in section IV, for the turbulence intensities in section V, and for the energy spectra in section VI. Finally, we conclude in section VII.

II. THE NECESSITY OF WALL MODELS BEFORE SGS MODELS IN LES

Most SGS models assume that a considerable fraction of the kinetic energy (i.e., 80-90% [2]) is resolved by the grid, and the Reynolds number and grid resolutions must comply with this requirement in order to faithfully assess the performance of the models. In unbounded flows like isotropic turbulence, LES can be computed at relatively coarse grid resolutions while still meeting this condition. On the contrary, this condition is not as favorable for wall-bounded flows. The number of grid points N to compute a turbulent boundary layer of thickness δ spanning a wall-parallel area of $L_1 \times L_3$ is

$$N = \int_0^{L_1} \int_0^{\delta} \int_0^{L_3} \frac{dx_1 dx_2 dx_3}{\Delta_1 \Delta_2 \Delta_3}, \quad (1)$$

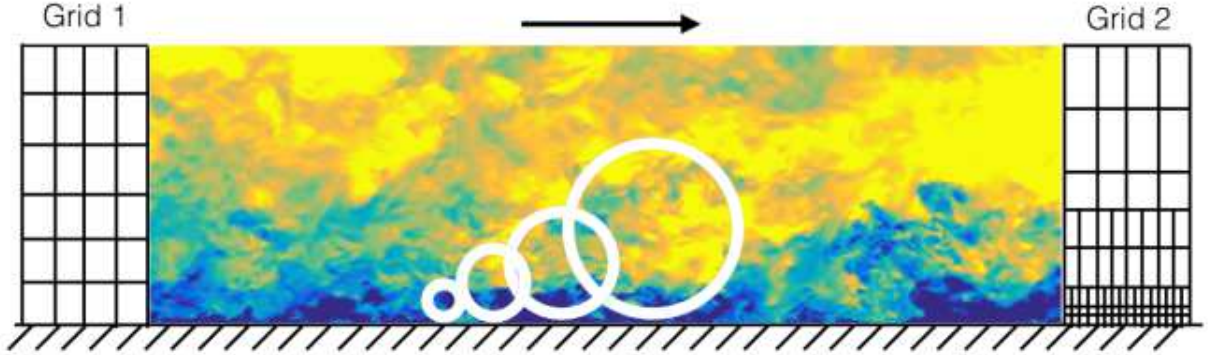


FIG. 1: Instantaneous streamwise velocity of a turbulent channel flow and sketch of wall-attached eddies of different sizes (white circles). Colors range from blue for low velocity to yellow for high velocity. Grid 1 (left) depicts a uniform grid typical of WMLES. Grid 2 (right) represents a nested grid necessary for proper WRLES.

where x_1 , x_2 and x_3 are the streamwise, wall-normal and spanwise directions, respectively, and Δ_1 , Δ_2 and Δ_3 are the target grid resolutions in each direction that may be a function of space. The required number of grid points can be expressed as $N \sim Re^\zeta$, where the exponent ζ depends on the sizes of the eddies expected to be accurately represented by the grid. Estimations of ζ can be found in Chapman [26] and Choi and Moin [27]. DNS aims to capture eddies in the dissipative range, and hence $\Delta_i \sim \eta$ and $\zeta \approx 2.6$, where η is the Kolmogorov length-scale. To resolve the energy-containing eddies as in classic LES (also referred to as wall-resolved LES, WRLES) it is necessary that $\Delta_i \sim L_\varepsilon$ which yields $\zeta \approx 1.9$, where L_ε is the integral length-scale. In the logarithmic region of wall-bounded flows, L_ε grows linearly with x_2 and the energy-containing eddies have sizes proportional to the distance to the wall [28, 29]. Consequently, the LES grid must be accordingly reduced in all spatial directions to resolve a constant fraction of the turbulent kinetic energy, increasing the computational cost. WRLES can be properly performed through nested grids [30] such as the one depicted in Fig. 1. Otherwise, the near-wall grid resolution does not suffice to capture the energy-containing eddies, and most SGS models perform poorly [31]. Finally, if we target to model only the outer motions (as in wall-modeled LES, WMLES), the grid requirements are such that $\Delta_i \sim \delta$, and $\zeta \leq 1$ depending on the wall model approach.

Although WRLES has been practiced for a long time, actual WRLES is scarce. Typically, only the wall-normal resolution is properly refined according to the size of the energy-containing eddies, while the wall-parallel directions remain under-resolved. Most of the grid convergence studies in wall-bounded LES mentioned in the introduction fall within this category. The consequence is that the majority of these validation works are at relatively low Reynolds numbers to make the computational cost of WRLES affordable [27] and avoid the errors of under-resolving the wall-parallel directions. However, it is questionable whether SGS models are active enough in these conditions to adequately measure their performance.

To illustrate the poor performance of SGS models when the near-wall region is under-resolved, Fig. 2 shows the mean streamwise velocity profile, $\langle \tilde{u}_1 \rangle$, for a turbulent channel flow as a function of the wall-normal distance x_2 , where $\langle \cdot \rangle$ denotes average in homogeneous directions and time, and (\cdot) is the resolved LES field. The details of the simulations are discussed in section III.2 (see Table I), but for now, it is only important to remark that all cases were computed using identical grids (with 13 points per boundary layer thickness, δ) and friction Reynolds number, $Re_\tau \approx 950$. Coarse DNS (no SGS model and no wall model) provides the worst prediction (squares in Fig. 2). Ideally, a perfect SGS model will supply the missing stresses at all distances from the wall. Indeed, Fig. 2 shows that the solution improves by introducing dynamic Smagorinsky model as SGS model (circles); however, the performance is still poor and $\langle \tilde{u}_1 \rangle$ is far from the reference DNS velocity profile. In contrast, the agreement with DNS is excellent when the equilibrium wall model from Kawai and Larsson [32] is applied (triangles), despite the fact that there is no explicit SGS model in this case (i.e., the numerical errors act as an implicit model).

Note that for all cases, the shape of $\langle \tilde{u}_1 \rangle$ far from the wall is barely affected and always very close to the DNS mean velocity profile, even when there is no SGS model due to the low Reynolds number. The main source of error comes from the inaccurate prediction of the wall friction velocity, u_τ , that translates into an overprediction of $\langle \tilde{u}_1^+ \rangle = \langle \tilde{u}_1 \rangle / u_\tau$. This suggests that the application of most common SGS models alone is not sufficient to provide the

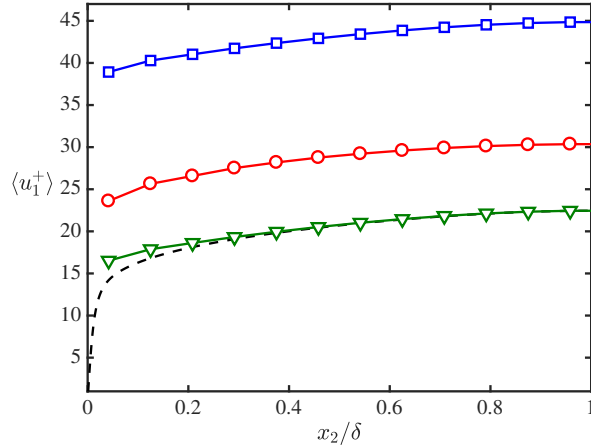


FIG. 2: Mean streamwise velocity profile, $\langle u_1^+ \rangle$, for a turbulent channel flow as a function of the wall-normal distance scaled with the channel half-height, x_2/δ . The cases plotted are: squares, no explicit SGS model with no-slip boundary condition (NM950-NS); circles, dynamic Smagorinsky model with no-slip boundary condition (DSM950-NS); triangles, no explicit SGS model with equilibrium wall model from Kawai and Larsson [32] (NM950-EQWM). All cases are at friction Reynolds number $Re_\tau \approx 950$. DNS is dashed line. More details are provided in table I.

correct stress at the wall, and only by means of a wall model can the problem be attenuated. The result highlights the rarely mentioned fact that, for increasing Re or coarsening of grid resolution, wall models are needed before SGS models, at least regarding the prediction of the mean velocity profile. The rationale behind this requirement is simple: the energy-containing eddies are smaller as they get closer to the wall, and without any *a priori* knowledge of the flow or without the necessary computational power, the near-wall layer is the first region to become under-resolved.

The problem would be alleviated by performing true WRLES with three-dimensional refinement as the grid approaches the wall as the Grid 2 in Fig. 1. However, this is an uncommon practice due to the complexity of the implementation and most attempts at WRLES suffer at some degree from the limitation demonstrated in Fig. 2. Therefore, it is important to emphasize that, in wall-bounded flows, the testing and validation of SGS is contaminated (and probably dominated) by the errors accumulated near the wall, and many of the mismatches of mean velocity profiles between DNS and LES reported in the literature are probably caused by the necessity of wall models before SGS models. It is necessary to remark that we do not advocate for LES without a SGS model, but we only emphasize the fact that validation at low Reynolds numbers or very fine grid resolutions could be less meaningful due to inactive SGS models far from the wall and the predominance of the near-wall errors. The behavior of SGS models close to the wall has been improved by recent works such as constrained LES [33], integral length-scale approximation models [34], and explicit algebraic models [35], among others. These approaches reduce substantially the grid requirements by modifying the SGS model near the wall while still maintaining the no-slip boundary condition. Nevertheless, the present work is focused on the error analysis within the outer flow far from the wall, and the aforementioned SGS models will not be considered.

III. BENCHMARK FOR THE OUTER REGION OF WALL-BOUNDED TURBULENCE

III.1. Exact mean wall-stress turbulent channel flows

We consider a plane turbulent channel flow with periodic streamwise and spanwise directions. The incompressible LES equations are obtained by applying a spatial filter to the Navier–Stokes equations,

$$\frac{\partial \bar{u}_i}{\partial t} + \frac{\partial \bar{u}_i \bar{u}_j}{\partial x_j} + \frac{\partial \tau_{ij}}{\partial x_j} = -\frac{1}{\rho} \frac{\partial \bar{p}}{\partial x_i} + \nu \frac{\partial^2 \bar{u}_i}{\partial x_j \partial x_j}, \quad \frac{\partial \bar{u}_i}{\partial x_i} = 0, \quad (2)$$

where \bar{u}_i for $i = 1, 2, 3$ are the streamwise, wall-normal and spanwise filtered velocities, respectively, \bar{p} is the filtered pressure, $\tau_{ij} = \bar{u}_i \bar{u}_j - \bar{u}_i \bar{u}_j$ is the effect of the sub-filter scales on the resolved eddies, ρ is the flow density, and ν is the kinematic viscosity. The streamwise, wall-normal and spanwise spatial directions are x_i for $i = 1, 2, 3$, respectively, and the walls are located at $x_2 = 0$ and $x_2 = 2\delta$. The objective of LES modeling is to approximate τ_{ij} via the SGS

tensor τ_{ij}^{SGS} . To emphasize that an LES model is not exact, the resolved LES velocity is denoted by \tilde{u}_i and we expect that $\tilde{u}_i \approx \bar{u}_i$ for an accurate SGS model.

We have acknowledged in section II the necessity of benchmarks for wall-bounded turbulence that are independent of the strict near-wall resolution requirements. To attain this goal, the no-slip boundary condition at the wall is replaced by a constant wall-stress condition imposed through a Neumann boundary condition of the form

$$\frac{\partial \tilde{u}_1}{\partial n} \Big|_w = \frac{\tau_w - \tau_{12}^{\text{SGS}}|_w}{\nu}, \quad (3)$$

where w denotes quantities evaluated at the wall, n is the wall-normal direction oriented towards the interior of the channel, and τ_w is the mean wall stress known *a priori* from DNS such that (3) can be thought of as a wall-model supplying the exact mean wall stress. It has been shown before that imposing the correct mean wall stress is sufficient to predict one-point statistics accurately in WMLES [36].

The set-up above is not intended to capture the near-wall dynamics, and the small eddies close to the wall are prone to be misrepresented when (2) is discretized for coarse grid resolutions. However, our focus is on the outer flow along the range $0.2\delta < x_2 < \delta$ [37], and previous studies have revealed that the flow statistics and structure of this region are relatively independently of the particular configuration of the eddies closest to the wall, even if they are partially or completely under-resolved. Some examples are the roughness experiments in channels and boundary layers [38, 39, 40, 41, 42], and the idealized numerical studies by Flores and Jiménez [41], Mizuno and Jiménez [43], Chung et al. [44] and Lozano-Durán and Bae [45], among others. In all these cases, the near-wall region was seriously modified or directly bypassed, but the properties of the outer layer remained essentially unaltered. Therefore, the correct representation of the outer layer dynamics remains uncoupled from the inner layer structure, supporting the numerical experiment presented here as a valid framework to assess LES errors far from the wall.

III.2. Numerical experiments

We perform a set of LES of plane turbulent channels driven by a constant mass flow in the streamwise direction. The simulations are computed with a staggered second-order finite difference [46] and fractional-step method [47] with a third-order Runge-Kutta time-advancing scheme [48]. The code has been validated in previous studies in turbulent channel flows [49, 50] and flat-plate boundary layers [51]. Periodic boundary conditions are imposed in the streamwise and spanwise directions, while for the top and bottom walls we use either the no-slip (NS) boundary condition or exact-wall-stress (EWS) Neumann boundary condition from (3).

Two SGS models are investigated: dynamic Smagorinsky model (DSM) [10, 52] and anisotropic minimum dissipation (AMD) model [53], which are regarded as representative of eddy viscosity models with and without test filtering, respectively. We will also consider cases without an explicit SGS model (NM) where the numerical truncation errors act as an implicit SGS model. Some of our results have also been computed for the Vreman model [54] whose performance was found to be similar to AMD and consistent with our conclusions below.

The size of the computational domain is $8\pi\delta \times 2\delta \times 3\pi\delta$ in the streamwise, wall-normal and spanwise directions, respectively. The grid resolutions are denoted by Δ_1, Δ_2 , and Δ_3 for the respective spatial directions, and they range from 0.025δ to 0.2δ corresponding to 5 to 40 points per boundary layer thickness. These numbers are in accordance with our range of interest, i.e., the characteristic grid resolutions encountered in WMLES of real external aerodynamic applications, and fall within the recommendations by Chapman [26] for resolving the large eddies in the outer region of the boundary layer. Four different friction Reynolds numbers are considered, $Re_\tau = u_\tau \delta / \nu \approx 950, 2000, 4200$ and 8000 , where u_τ is the friction velocity at the wall. The LES results are compared with reference DNS data from Hoyas and Jiménez [55], Lozano-Durán and Jiménez [56], and Yamamoto and Tsuji [57]. All the LES channel flow simulations were run at least for $100\delta/u_\tau$ after transients.

The list of cases used to motivate the need of wall models in section II is given in table I. The simulations discussed for the remainder of the paper are named following the convention [SGS model][Re_τ]-[boundary condition]-[grid resolution], where the grid resolutions are denoted by i1, i2, i3 and i4 for isotropic grids, and by a1, a2 and a3 for anisotropic grids. The different grid resolutions are provided in table II. For example, DSM4200-EWS-i2 is an LES with DSM at $Re_\tau \approx 4200$ with EWS boundary condition and grid resolutions $\Delta_1 = \Delta_2 = \Delta_3 = 0.1\delta$.

IV. ERROR SCALING OF THE MEAN VELOCITY PROFILE

The mean velocity profile is examined first as it is the figure of merit for most LES studies. We will assume that $\langle u_1 \rangle \approx \langle \bar{u}_1 \rangle$ and hence, the LES mean velocity can be directly compared with unfiltered DNS data. The approximation

Case	SGS model	Wall condition	Re_τ	Δ_1/δ	Δ_2/δ	Δ_3/δ
NM950-NS	NM	NS				
DSM950-NS	DSM	NS	932	0.10	0.080	0.050
NM950-EQWM	NM	EQWM				

TABLE I: List of cases used in section II. The second column contains the SGS model: no explicit SGS model (NM) or dynamic Smagorinsky model (DSM). The third column refers to the wall boundary condition: no-slip (NS) or Neumann boundary condition using the equilibrium wall-model from Kawai and Larsson [32] (EQWM). The fourth column indicates the friction Reynolds number. Δ_1 , Δ_2 and Δ_3 are the streamwise, wall-normal and spanwise grid resolutions respectively.

Grid resolution label	Δ_1/δ	Δ_2/δ	Δ_3/δ
i1	0.20	0.20	0.20
i2	0.10	0.10	0.10
i3	0.050	0.050	0.050
i4	0.025	0.025	0.025
a1	0.20	0.10	0.05
a2	0.10	0.10	0.07
a3	0.20	0.10	0.10

TABLE II: Tabulated list of resolutions as a fraction of the channel half-height, δ . The first column contains the label used for naming the LES cases computed with different grids. Δ_1 , Δ_2 and Δ_3 are the streamwise, wall-normal and spanwise grid resolutions, respectively.

is reasonable when the quantity averaged is dominated by large-scale content, as it is the case for $\langle u_1 \rangle$. In particular, the error for the mean velocity profile is systematically quantified as the average difference between the LES solution and the corresponding DNS in the outer region as

$$\mathcal{E}_m = \left[\frac{\int_{0.2\delta}^{\delta} (\langle \tilde{u}_1 \rangle - \langle u_1 \rangle)^2 dx_2}{\int_{0.2\delta}^{\delta} \langle u_1 \rangle^2 dx_2} \right]^{1/2}, \quad (4)$$

where $\langle u_1 \rangle$ is evaluated from DNS data. The choice excludes the nonphysical/under-resolved range $x_2 < 0.2\delta$ for the LES cases using the exact-wall-stress approach as discussed in section III.1. For a channel flow driven by constant mass flux and exact mean wall-stress, some reference errors can be obtained by two extreme cases, i.e., a fully turbulent profile defined by the flat velocity $\langle \tilde{u}_1 \rangle = Q/2\delta$, and the laminar solution represented by the parabolic function $\langle \tilde{u}_1 \rangle = 3Q/4\delta(2 - x_2/\delta)x_2/\delta$, whose errors are $\mathcal{E}_{m,turb} \approx 0.06$ and $\mathcal{E}_{m,lam} \approx 0.26$, respectively.

In general, the error will depend on the grid resolution and Reynolds number,

$$\mathcal{E}_m = \mathcal{E}_m(\Delta_1, \Delta_2, \Delta_3, Re_\tau), \quad (5)$$

and if we further assume that $\mathcal{E}_m \sim \Delta^{\alpha_m} Re_\tau^{\gamma_m}$, where Δ is a (yet to define) measure of the grid size, the exponents α_m and γ_m can be theoretically estimated from the error equation and empirically computed from numerical experiments. Both analysis are performed below. Ultimately, we will conclude that LES is a viable approach for computing the outer flow of wall-bounded flows if the empirical values of the exponents are such that $\alpha_m > 0$ and $\gamma_m \approx 0$.

IV.1. Theoretical estimations

We estimate the expected error behavior of \mathcal{E}_m for a generic SGS that will serve as a reference for the numerical observations in the next section. Let us consider the exact relation between the filtered and unfiltered velocities at a location x_2^o obtained from the integrated mean momentum equation for \bar{u}_1 and u_1 ,

$$\langle \bar{u}_1 \rangle - \langle u_1 \rangle = u_w + \frac{1}{\nu} \int_0^{x_2^o} \langle \bar{u}'_1 \bar{u}'_2 - u'_1 u'_2 + \tau_{12} \rangle dx_2, \quad (6)$$

where $(\cdot)'$ denotes fluctuating quantities and u_w is the mean filtered velocity at the wall. For a symmetric filter with well-defined non-zero second moment in real space, τ_{12} can be written as [58]

$$\tau_{12} \approx \frac{\partial \bar{u}_1}{\partial x_i} \frac{\partial \bar{u}_2}{\partial x_i} \bar{\Delta}_i^2 + \mathcal{O}(\bar{\Delta}_1^4 + \bar{\Delta}_2^4 + \bar{\Delta}_3^4), \quad (7)$$

where repeated indices imply summation, and $\bar{\Delta}_i$ signifies the filter size in the i -th direction defined as the square root of the second moment of the filter operator

$$\bar{\Delta}_i^2 = \int_{-\infty}^{\infty} \int_{-\infty}^{\infty} \int_{-\infty}^{\infty} x_i^2 G(x_1, x_2, x_3) dx_1 dx_2 dx_3. \quad (8)$$

G is the filter kernel and $\bar{\Delta}_i^2 = \bar{c} \Delta_i^2$, where \bar{c} is a coefficient that depends on the particular filter shape, e.g., for a box filter $\bar{c} = 1/12$. For the rest of the argument, we will neglect terms of the order of $\mathcal{O}(\bar{\Delta}_i^4)$, namely, we assume that traditional SGS models are a fourth order approximation to τ_{ij} . The simplification will be useful for estimating the error scaling independently of any particular SGS model.

Analogously, the difference of the filtered and unfiltered fluctuating tangential stresses can be approximated by

$$\bar{u}'_1 \bar{u}'_2 - u'_1 u'_2 = \frac{\bar{\Delta}_i^2}{2} \left(\bar{u}'_1 \frac{\partial^2 \bar{u}'_2}{\partial x_i^2} + \bar{u}'_2 \frac{\partial^2 \bar{u}'_1}{\partial x_i^2} \right) + \mathcal{O}(\bar{\Delta}_1^4 + \bar{\Delta}_2^4 + \bar{\Delta}_3^4). \quad (9)$$

From (6), (7) and (9), the error in the mean velocity profile can be shown to follow

$$\mathcal{E}_m \sim \langle \bar{u}_1 \rangle - \langle u_1 \rangle \sim \int_0^{x_2^o} \left\langle \bar{\Delta}_i^2 \frac{\partial \bar{u}_1}{\partial x_i} \frac{\partial \bar{u}_2}{\partial x_i} + \frac{\bar{\Delta}_i^2}{2} \left(\bar{u}'_1 \frac{\partial^2 \bar{u}'_2}{\partial x_i^2} + \bar{u}'_2 \frac{\partial^2 \bar{u}'_1}{\partial x_i^2} \right) \right\rangle dx_2. \quad (10)$$

Note that the filter sizes in (10) are arranged in the form $\bar{\Delta}_i^2 \sim \Delta_i^2$ and such that $\mathcal{E}_m \sim (\Delta_i \Delta_i)^{\alpha_m/2}$, which motivates the use of the L_2 -norm of $(\Delta_1, \Delta_2, \Delta_3)$ as the characteristic grid-size as long as the error is measured according to (4). Eq. (10) also shows that Δ_i do not provide a full description of the error, and that a complete characterization will involve an effective grid size

$$\Delta_{\text{eff}} = \sqrt{d_1 \Delta_1^2 + d_2 \Delta_2^2 + d_3 \Delta_3^2}, \quad (11)$$

where d_k , $k = 1, 2, 3$, are flow dependent functions from (10).

Equation (10) can be further exploited to determine the scaling of \mathcal{E}_m with Δ by approximating the dependence of \bar{u}'_i , $\frac{\partial^2 \bar{u}'_i}{\partial x_i \partial x_i}$ and $\frac{\partial \bar{u}_i}{\partial x_i}$ on Δ . A rough estimation may be performed by assuming the kinetic energy spectrum $E_K \sim k^\beta$, with the wavenumber $k \sim 1/\Delta$, and the isotropic velocity gradient $G = \partial u / \partial x$ at scale Δ such that

$$\bar{u}'_{1,2} \frac{\partial^2 \bar{u}'_{2,1}}{\partial x_i \partial x_i}, \frac{\partial \bar{u}_1}{\partial x_i} \frac{\partial \bar{u}_2}{\partial x_i} \sim G^2 \sim \frac{u^2}{\Delta^2} \sim \frac{k E_K}{\Delta^2} \sim \Delta^{-(\beta+3)}, \quad (12)$$

where the exponent β depends on the regime the SGS models operates: for the shear-dominated range $\beta = -1$ [38] and $G^2 \sim \Delta^{-2}$, whereas for the inertial range $\beta = -5/3$ [59] and $G^2 \sim \Delta^{-4/3}$. Taking into account the scaling above and after integration of the right-hand side in (10), the expected error in the LES mean velocity profile should scale as

$$\mathcal{E}_m^s \sim \Delta, \quad \mathcal{E}_m^i \sim \Delta^{5/3}, \quad (13)$$

for SGS models acting on the shear-dominated or inertial regimes, respectively. The scaling of \mathcal{E}_m with Δ in (13) can be estimated from simpler dimensional arguments without going through (10), but it was beneficial to write the explicit equation of the error to obtain more information about the functional form. Nevertheless, it is important to remark that (13) should be understood as a rough estimation since the actual errors evolve according to a non-linear equation and, hence, their rigorous mathematical treatment is highly elusive. This consideration is also applicable to the error estimations for the turbulence intensities and energy spectra in later sections.

IV.2. Numerical assessment

Fig. 3 shows the mean velocity profiles for a selection of cases at $Re_\tau \approx 4200$ for different grid resolutions without SGS model (Fig. 3a) and with DSM (Fig. 3b). As expected, $\langle \tilde{u}_1 \rangle$ converges to $\langle u_1 \rangle$ as the grid is refined for cases with DSM (equivalently for AMD), while the trend is more inconsistent for cases without explicit SGS model.

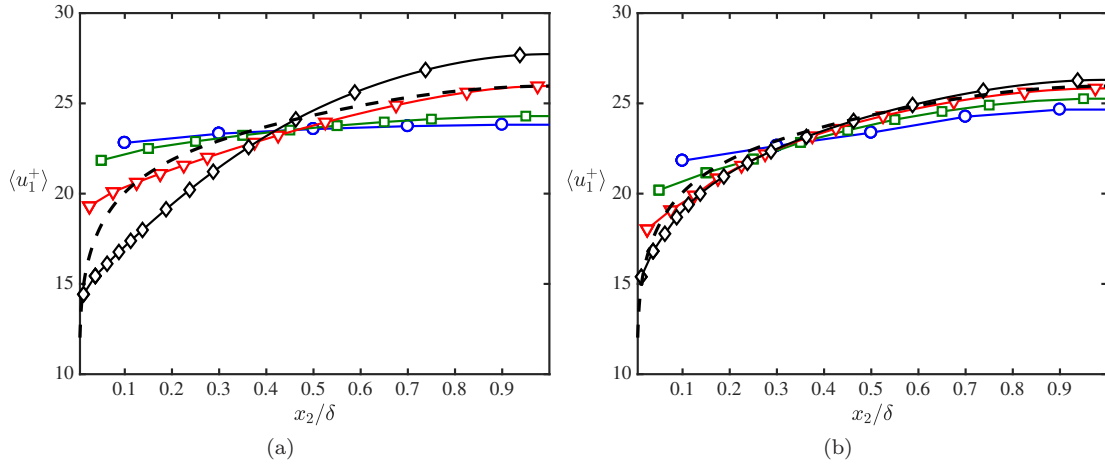


FIG. 3: Mean streamwise velocity profile at $Re_\tau \approx 4200$ for (a) no explicit SGS model, and (b) DSM. Symbols are for grids i1 (circles), i2 (squares), i3 (triangles), and i4 (diamonds) from table II. The dashed line is DNS.

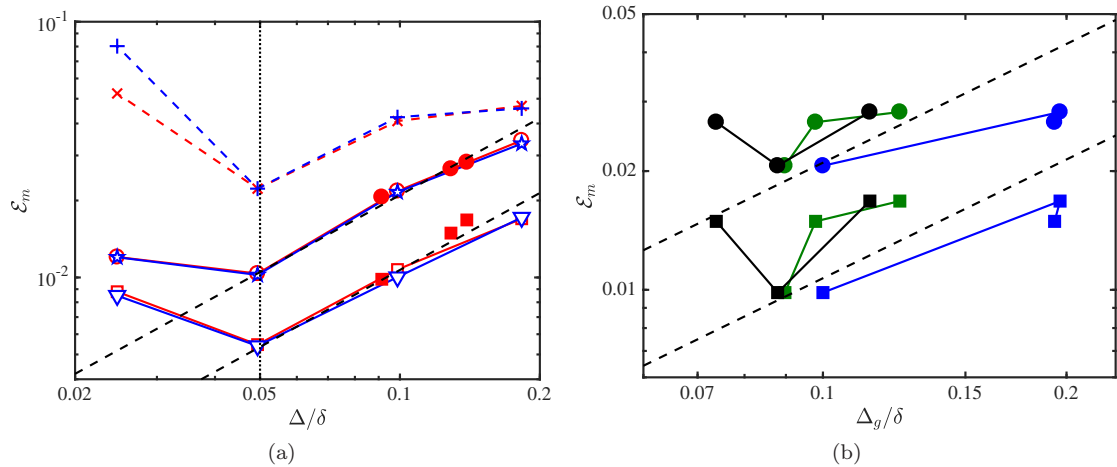


FIG. 4: (a) Error in the mean velocity profile as a function of the characteristic grid resolution $\Delta = \sqrt{(\Delta_1^2 + \Delta_2^2 + \Delta_3^2)/3}$. Colors are: red, cases at $Re_\tau \approx 4200$; blue, cases at $Re_\tau \approx 8000$. Symbols are: circles and stars, DSM; triangles and squares, AMD; \times and $+$, no explicit SGS model. Open and closed symbols are for isotropic and anisotropic grids, respectively. Dashed lines are $\mathcal{E}_m = 0.107\Delta/\delta$ and $\mathcal{E}_m = 0.210\Delta/\delta$, and dash-dotted line is $\Delta/\delta = 0.05$. (b) Alternative characteristic grid sizes: $\Delta_g = \sqrt[3]{\Delta_1\Delta_2\Delta_3}$ (green), $\Delta_g = \max(\Delta_1, \Delta_2, \Delta_3)$ (blue), and $\Delta_g = \sqrt{3/(1/\Delta_1^2 + 1/\Delta_2^2 + 1/\Delta_3^2)}$ (black). Cases are DSM (circles) and AMD (squares) for anisotropic grids at $Re_\tau \approx 4200$. For reference, we have also included the dashed lines from (a).

The quantitative assessment of the \mathcal{E}_m is shown in Fig. 4(a) as a function of the characteristic grid resolution Δ , taken to be

$$\Delta = \sqrt{\frac{\Delta_1^2 + \Delta_2^2 + \Delta_3^2}{3}}, \quad (14)$$

as motivated by (10). Other grid definitions were also inspected such as the cube root of the cell volume [60, 61], the maximum of the grid sizes [62], or the square root of the harmonic mean of the squares of the grid sizes (all reported in Fig. 4b), among others. However, the best collapse is found for definition (14), in accordance with the discussion in section IV.1. A survey of existing subgrid length-scales can be found in Trias et al. [63] but note that in the current study we are discussing the most meaningful grid size to characterize \mathcal{E}_m , that does not need to coincide with the characteristic length-scale embedded in SGS models (i.e., $\tilde{\Delta}$ in the Smagorinsky model $-2C_s\tilde{\Delta}^2\sqrt{2\tilde{S}_{nm}\tilde{S}_{nm}}\tilde{S}_{ij}$, where \tilde{S}_{ij} is the resolved rate-of-strain tensor and C_s is a constant).

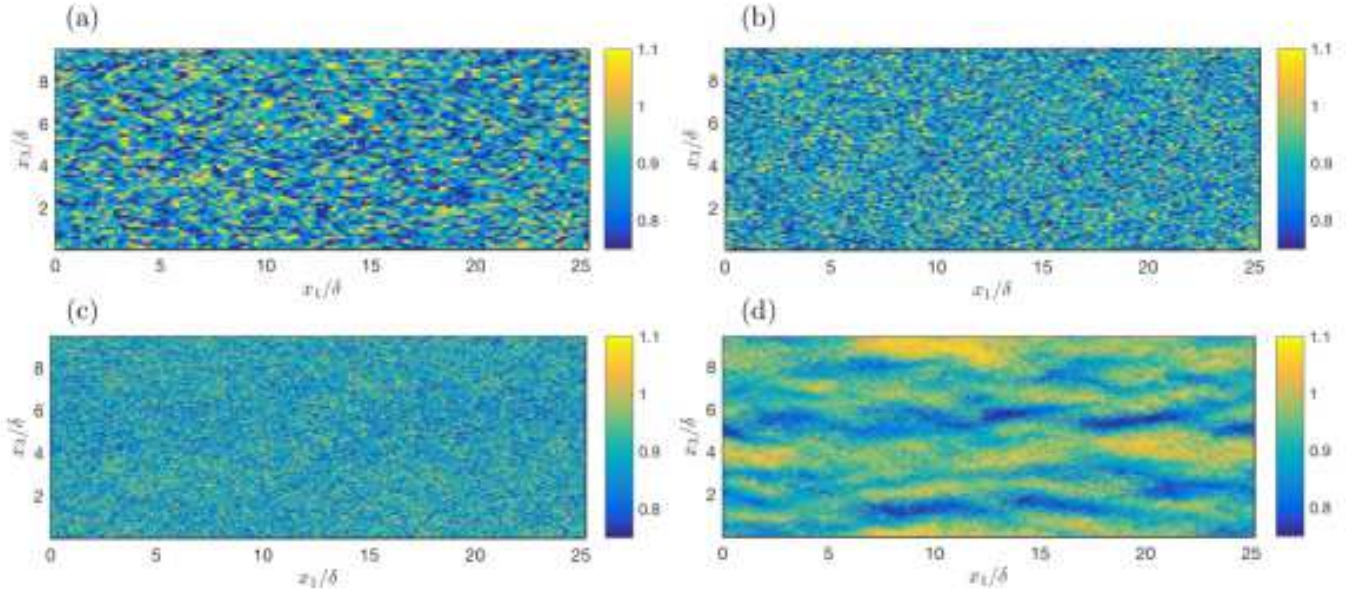


FIG. 5: Instantaneous snapshots of the streamwise velocity in a wall-parallel plane at $x_2 \approx 0.5\delta$ for (a) NM4200-EWS-i1, (b) NM4200-EWS-i2, (c) NM4200-EWS-i3, (d) NM4200-EWS-i4.

The errors for cases without SGS model are discernibly larger than those calculated with DSM or AMD, especially for the finer grid resolutions, and similar to those for fully turbulent flows ($\mathcal{E}_{m,turb} \approx 0.06$). Moreover, they follow a non-monotonic behavior with Δ , inconsistent with the second-order prediction from the linear analysis of the spatial discretization errors, probably because such an approximation holds for $\Delta \rightarrow 0$ but it is no longer representative of errors subjected to non-linear diffusion and convection for $\Delta \sim \delta$. Visual inspection of the instantaneous streamwise velocity fields for cases without SGS model in Fig. 5 shows that there is a substantial change in the flow topology at $\Delta \approx 0.05\delta$. For $\Delta > 0.05\delta$, the velocity field lacks the characteristic turbulence features and exhibits instead a highly mixed and disorganized structure (Figs. 5a–c). On the other hand, clearly defined streamwise velocity streaks emerge for $\Delta < 0.05\delta$ (Fig. 5d). The physical justification for the existence of this critical grid resolution for cases without SGS model is relegated to the spectra analysis in section VI, but for now we can argue that these streaks are nonphysical in the sense that they worsen the mean velocity profile prediction as shown in Fig. 3(a) for NM4200-EWS-i4. For cases with SGS model, streaks are always present in the flow at all grid resolutions (not shown), but we can hypothesize that the effect described for cases without SGS model still affects the convergence of the solution. This suggests that the errors reported in Fig. 4(a) should be separated into two different regimes delimited by $\Delta \approx 0.05\delta$.

For cases with SGS model and $\Delta > 0.05\delta$, the error follows

$$\mathcal{E}_m \approx \epsilon \left(\frac{\Delta}{\delta} \right) Re_\tau^0, \quad (15)$$

where ϵ is a model dependent constant. The results show that the LES solution converges to the correct value free from viscous effects, $\mathcal{E}_m \sim Re_\tau^0$ (given a perfect wall model for the mean) as demanded from a proper LES far from the walls. Our results also suggest that $\mathcal{E}_m \sim \Delta$, which agrees well with the theoretical estimation \mathcal{E}_m^s discussed in section IV.2. Although both DSM and AMD converge at the same rate with Δ , the prefactor ϵ can play an important role in the error magnitude and thus different models may be preferred due to its lower ϵ . The results in appendix VII show that similar conclusions are drawn for the Vreman model.

For $\Delta < 0.05\delta$, the errors depart from $\mathcal{E}_m \sim \Delta$ and saturate, probably due to the competing effects of the improved prediction by the SGS model versus the formation of nonphysical flow structures discussed in Fig. 5. Some additional test cases included in appendix VII suggest that $\mathcal{E}_m \sim \Delta$ is recovered for finer grids. However, the convergence of $\langle \tilde{u}_1 \rangle$ to the DNS solution may entail an intricate non-monotonic response as reported in Meyers and Sagaut [16] for grids much finer than those typical of WRLES.

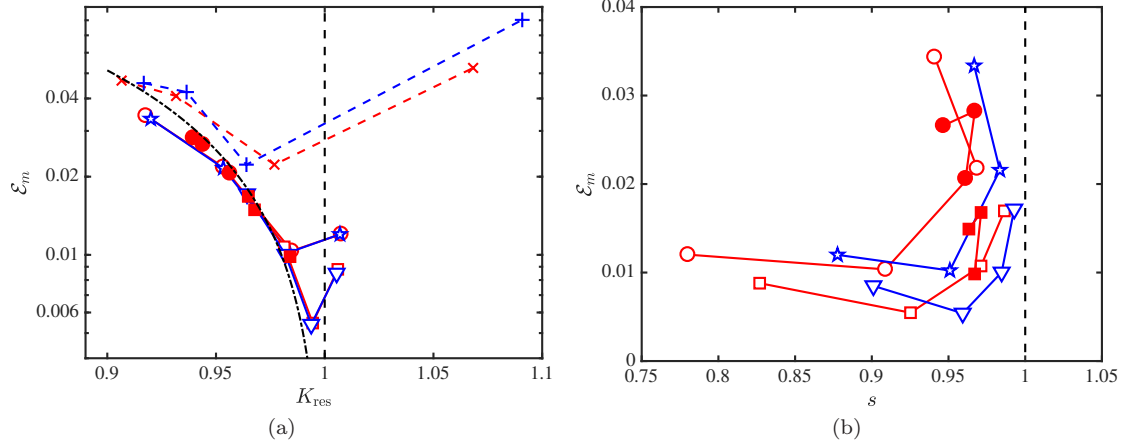


FIG. 6: Error in the mean streamwise velocity profile as a function of (a) the resolved total kinetic energy, and (b) SGS activity parameter. Colors are: red, cases at $Re_\tau \approx 4200$; blue, cases at $Re_\tau \approx 8000$. Symbols are: circles and stars, DSM; triangles and squares, AMD; \times and $+$, no explicit SGS model. Open and closed symbols are for isotropic and anisotropic grids, respectively. The dash-dotted line in (a) is $K_{\text{res}} \approx (1 - \mathcal{E}_m)^2$. The vertical dashed lines are $K_{\text{res}} = 1$ and $s = 1$.

Alternative metrics to functionally quantify \mathcal{E}_m are the resolved total kinetic energy,

$$K_{\text{res}} = \frac{\langle \tilde{u}_i \tilde{u}_i \rangle}{\langle u_i u_i \rangle}, \quad (16)$$

and the SGS activity parameter [13, 21],

$$s = \frac{\langle 2\nu_t \tilde{S}_{ij} \tilde{S}_{ij} \rangle}{\langle 2\nu_t \tilde{S}_{ij} \tilde{S}_{ij} + 2\nu \tilde{S}_{ij} \tilde{S}_{ij} \rangle}, \quad (17)$$

where ν_t is the eddy viscosity. The results are shown in Fig. 6 where K_{res} and s are averaged over the wall-normal range $[0.3\delta, \delta]$. Despite the coarse grid resolutions investigated in the present work, the resolved kinetic energy remains above 90% for all cases (Fig. 6a) and emerges as a highly effective metric to assess the errors in the mean profile even among different SGS models. The result is not surprising since K_{res} can be easily related to \mathcal{E}_m if we assume that $\langle u_1^2 \rangle / \langle u_i^2 \rangle \gg 1$ for $i = 2, 3$, and $\langle u_i^2 \rangle \approx \langle u_i \rangle^2$. The former are usually ~ 100 , while the last condition is reasonably well satisfied if u_1 is close to a normal distribution $\mathcal{N}(\mu, \sigma)$ with mean μ and standard deviation σ such that $\mu/\sigma \gg 1$, that can be shown to be the case for high-Reynolds-number turbulent channel flows. Under those conditions, the resolved kinetic energy can be expressed as

$$K_{\text{res}} \approx (1 - \mathcal{E}_m)^2, \quad (18)$$

which is included in Fig. 6(a) and shows an excellent agreement with the data. Therefore, \mathcal{E}_m and K_{res} are interchangeable metrics for characterizing errors in $\langle \tilde{u}_1 \rangle$. Cases with no explicit model do not follow the trend, and K_{res} can even exceed unity due to nonphysical velocity fluctuations whose origin is discussed in more detail in section V. The same effect is observed for cases with SGS models for the finest grid resolution but in a much lesser degree. The SGS activity is plotted in Fig. 6(b). Increasing s is associated with increasing \mathcal{E}_m , although the results are Reynolds number and SGS model dependent and do not collapse for isotropic and anisotropic grids. Nevertheless, (17) does not make use of DNS data, and it is a more realistic estimator for practical applications where the reference DNS solution is not available.

IV.3. Relevant length-scale for local error quantification

The error quantified above is an integrated measure across the entire outer layer and, consistently, the grid resolution was non-dimensionalized by the boundary layer thickness δ . However, the length-scale of the energy-containing eddies (L) is a function of the wall-normal direction, and local errors at a given x_2 are expected to vary accordingly. We

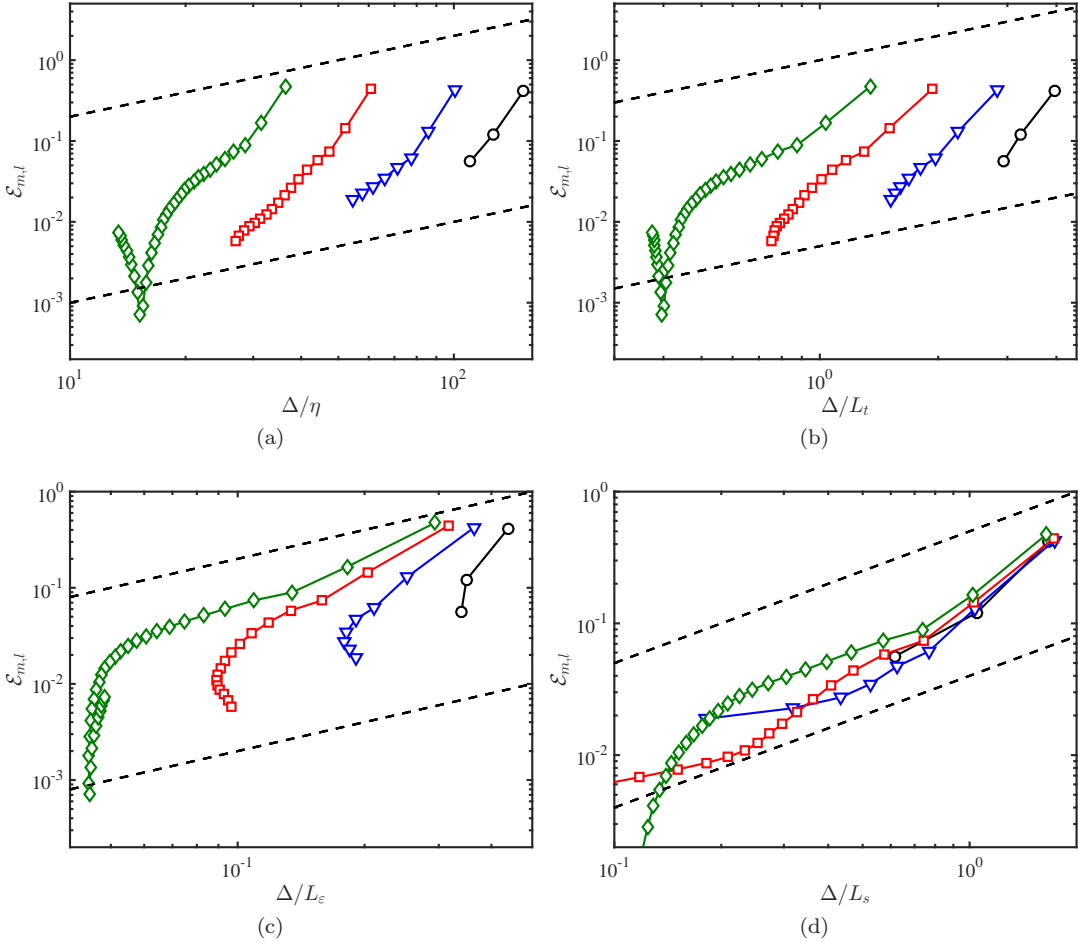


FIG. 7: Local error in the mean velocity profile as a function of Δ normalized by (a) Kolmogorov scale η , (b) Taylor microscale L_t , (c) integral length-scale L_ε , and (d) shear length-scale L_s . Cases are AMD4200-EWS-i1 (circles, black), AMD4200-EWS-i2 (triangles, blue), AMD4200-EWS-i3 (squares, red), and AMD4200-EWS-i4 (diamonds, green). Dashed lines are $\mathcal{E}_{m,l} \sim \Delta/L$ with $L = \eta, L_t, L_\varepsilon$ and L_s for (a), (b), (c) and (d), respectively.

investigate the physical length-scale relevant for local error scaling and define the x_2 -dependent error in the mean velocity profile as

$$\mathcal{E}_{m,l}(x_2) = \left(\frac{\int_{x_2-d}^{x_2+d} (\langle \tilde{u}_1 \rangle - \langle u_1 \rangle)^2 dx_2}{\int_{0.2\delta}^{\delta} \langle u_1 \rangle^2 dx_2} \right)^{1/2}, \quad (19)$$

where the integration limits, $x_2 \pm d$, coincide with the grid locations of \tilde{u}_1 , and the integral is numerically performed using the trapezoidal rule. Different candidates for L are tested, namely, the Kolmogorov scale $\eta = (\nu^3/\varepsilon)^{1/4}$ [37], the Taylor microscale $L_t = (15\nu \langle u'_i u'_i \rangle / \varepsilon)^{1/2}$ [64], the integral length-scale $L_\varepsilon = (K/3)^{3/2}/\varepsilon$ [37], and the shear length-scale $L_s = u_\tau (\partial \langle u_1 \rangle / \partial x_2)^{-1}$ [45, 65], where ε is the rate of energy dissipation, K is the turbulent kinetic energy, and $(\cdot)'$ denotes fluctuating quantities. All the length-scales are computed for the reference DNS data. The results for AMD4200-EWS-i1,i2,i3,i4 are shown in Fig. 7, and the best collapse is found for Δ/L_s . Similar results are obtained for the corresponding DSM cases except for the first off-wall grid point (not shown). The local error lies below 10% when the grid resolution is at least 0.5 times smaller than L_s , and it drastically drops for $\Delta < 0.2L_s$, although these ranges should be understood as tentative estimates. The results are also consistent with the excellent agreement with Δ/δ shown in Fig. 4 for the global error \mathcal{E}_m , and the universality of the mean velocity profile in the outer layer would suggest that the average integrated effect of L_s is proportional to δ since $(L_s)_{\text{avg}} = 1/0.8\delta \int_{0.2\delta}^{\delta} L_s(x_2) dx_2 \sim \delta$. For instance, under the rough assumption that there is no wake effect and the log-layer is valid until the edge of the boundary layer, then $(L_s)_{\text{avg}} \approx 0.25\delta$.

The largest errors are obtained for $\Delta/L_s > 1$, which correspond to the first off-wall grid points. We can argue that

close to the wall $L_s \approx \kappa x_2$, where κ is the von Kármán constant, and given that the third grid point is always at $x_2 = 2\Delta$, then $\Delta/L_s \approx 1/(2 \cdot \kappa) \approx 1.25$ independently of Δ . Consequently, no improved predictions are expected in $\langle \tilde{u}_1 \rangle$ at the first off-wall grid points as Δ is refined until the grid resolution reaches the WRLES-like regime. A similar argument was provided by Larsson et al. [66] based on the size of wall-attached eddies across the logarithmic region.

V. ERROR SCALING OF TURBULENCE INTENSITIES

In the previous section we have measured the errors on $\langle \tilde{u}_1 \rangle$ by accepting without question that LES and DNS are directly comparable. The assumption is reasonable if the filtering operation has little impact on the mean of a variable ϕ , that is, $\langle \phi \rangle \approx \langle \tilde{\phi} \rangle$, and this is the case for the mean velocity profile even at coarse filter sizes. However, smaller-scale motions play a non-negligible role on $\langle u_i'^2 \rangle$, casting doubts regarding how to compare fairly LES and DNS. If LES is formally interpreted by means of a spatial low-pass filter [3, 60], the meaningful quantities to compare are the turbulence intensities of the filtered DNS velocities. There are two caveats in order to carry on such comparison. First, although numerical differentiation has a low-pass filtering effect and the finite grid resolution prevents the formation of small scales, the filter operator is not distinctly defined in implicitly-filtered LES [67, 68, 69] and, consequently, neither is the associated filter size. The second caveat is probably more important: in real-world applications we are interested in predicting DNS values, whereas their filtered counterparts are of less practical importance.

In this section, we argue first the physical mechanism regulating the magnitude of the fluctuating velocities in implicitly-filtered LES. Secondly, we study the theoretical and numerical convergence of the LES turbulence intensities in wall-bounded flows.

V.1. The mechanism controlling fluctuating velocities in implicitly-filtered LES

Fig. 8(a) shows the root-mean-squared (rms) of the streamwise fluctuating velocity for DNS, LES without SGS model, and LES with DSM. In the absence of model, the LES intensities are over-predicted compared with DNS and, conversely, under-predicted with DSM. Similar results are obtained for the wall-normal and spanwise velocity fluctuations. The change in magnitude of the LES rms fluctuating velocities can be easily understood through the energy equation integrated over the channel flow domain \mathcal{V} with volume V ,

$$\frac{u_\tau^2 Q V}{2\delta^2} = \int_{\mathcal{V}} (\nu + \nu_t) \left(\frac{\partial \tilde{u}_i}{\partial x_k} \frac{\partial \tilde{u}_i}{\partial x_k} + \frac{\partial \tilde{u}_i}{\partial x_k} \frac{\partial \tilde{u}_k}{\partial x_i} \right) dV. \quad (20)$$

Eq. (20) shows that the input power to maintain the mass flow Q must be dissipated by the viscous/SGS terms. In the DNS limit ($\nu_t = 0$) with fixed ν , this is achieved by the velocity gradients $\partial \tilde{u}_i / \partial x_k \sim \Delta u_c / l_c$, where Δu_c and l_c are the characteristic velocity difference and length of the smallest scales, respectively. In LES, the smallest available length-scale is limited by the grid resolution $l_c \approx \Delta$. Thus, the two possible mechanisms to maintain consistency with (20) are by $\nu_t > \nu$, or by augmenting Δu_c (and hence the turbulence intensities). If ν_t and $\partial \nu_t / \partial x_k$ are large enough, Δu_c is under-predicted with respect to DNS as illustrated in Fig. 8(a). Conversely, for LES without explicit SGS model ($\nu_t = 0$) the only possible scenario is increasing the turbulence intensities, consistent with Fig. 8(a). This shows that the mean LES kinetic energy can exceed the (filtered or unfiltered) mean DNS kinetic energy when SGS models are not dissipative enough (as in Fig. 6a), which may be problematic for LES quality assessment.

In summary, the physical mechanism regulating the magnitude of the fluctuating velocities in implicitly-filtered LES is related to the necessity of generating dissipative terms of the correct magnitude rather than by the (non-existent) filtering operation. Nevertheless, the results above shows that even if implicitly-filtered LES is not rigorously equivalent to the filtered Navier–Stokes equations, it does hold some resemblance in the sense that the values of ν_t providing the correct mean velocity profile are accompanied by lower rms velocities as it would be expected from the filtered DNS velocity field.

V.2. Theoretical estimations

The metric adopted to measure errors in the turbulence intensities is

$$\mathcal{E}_{f,i} = \left[\frac{\int_{0.2\delta}^{\delta} (\langle \tilde{u}_i'^2 \rangle - \langle u_i'^2 \rangle)^2 dx_2}{\int_{0.2\delta}^{\delta} \langle u_i'^2 \rangle^2 dx_2} \right]^{1/2}, \quad i = 1, 2, 3. \quad (21)$$

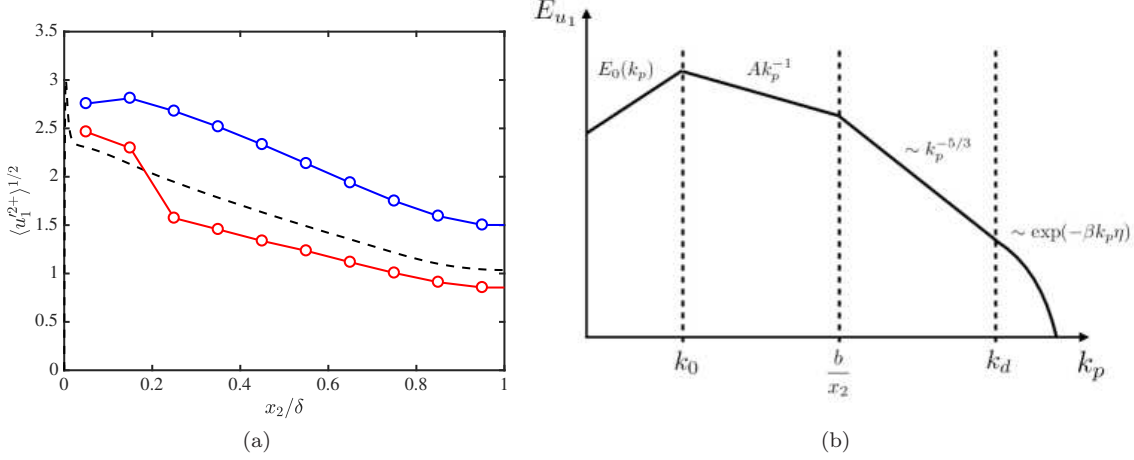


FIG. 8: (a) Streamwise rms velocity fluctuations at $Re_\tau \approx 4200$. Lines are: dashed, DNS; blue circles, NM4200-EWS-i2; red circles, DSM4200-EWS-i2. (b) Model spectrum for the streamwise turbulence intensity. The parameters A , b , k_0 , k_d and β are model constants.

For brevity, we will occasionally omit the subindex i when the particular component is not relevant in the discussion. Our goal is to estimate \mathcal{E}_f as a function of Δ .

In the logarithmic layer of wall-bounded turbulence at high Reynolds numbers, the intensities of the unfiltered velocity fluctuations are known to follow

$$\frac{\langle u_1'^2 \rangle}{u_\tau^2} = B_1 - A_1 \log\left(\frac{x_2}{\delta}\right), \quad \frac{\langle u_2'^2 \rangle}{u_\tau^2} = B_2, \quad \frac{\langle u_3'^2 \rangle}{u_\tau^2} = B_3 - A_3 \log\left(\frac{x_2}{\delta}\right), \quad (22)$$

where the coefficients B_i and A_i are constants considered to be universal for turbulent channel flows. Eq. (22) can be derived by using the attached-eddy hypothesis [70] or by dimensional analysis on the k^{-1} spectrum of u_1 and u_3 [38], and the blocking effect of the wall for u_2 . The hypothesis has been confirmed at high Reynolds number flows [71, 72] and it has also been clearly observed in the spanwise velocity and pressure fluctuations even for relatively low Reynolds numbers [73, 74, 75, 76]. An important consequence of (22) is that at a given x_2 in δ units, the magnitude of the velocity fluctuations scaled with u_τ is constant and independent of the Reynolds number.

We are now interested in the LES asymptotic high-Reynolds-numbers limit for the filtered fluctuating velocities $\langle \bar{u}_i'^2 \rangle$,

$$\frac{\langle \bar{u}_1'^2 \rangle}{u_\tau^2} = \bar{B}_1 - \bar{A}_1 f\left(\frac{x_2}{\delta}\right), \quad \frac{\langle \bar{u}_2'^2 \rangle}{u_\tau^2} = \bar{B}_2, \quad \frac{\langle \bar{u}_3'^2 \rangle}{u_\tau^2} = \bar{B}_3 - \bar{A}_3 f\left(\frac{x_2}{\delta}\right), \quad (23)$$

where \bar{B}_i and \bar{A}_i are constants that depend on Δ_i , and f is an unknown function such that $f(x_2) \rightarrow \log(x_2)$ as $\Delta_i \rightarrow 0$. The exact dependence of \bar{B}_i , \bar{A}_i on Δ_i , and the particular shape of f is expected to vary with the filter. The value of $\langle \bar{u}_i'^2 \rangle$ may be estimated for a symmetric filter with well-defined non-zero second moment in real space by considering [68, 77]

$$\langle \bar{u}_i'^2 \rangle = \langle \bar{u}_i'^2 \rangle - \Delta_k^2 \left\langle \left(\frac{\partial \bar{u}_i'}{\partial x_k} \right)^2 \right\rangle + \mathcal{O}(\Delta_1^4 + \Delta_2^4 + \Delta_3^4). \quad (24)$$

If we further assume that $\langle \bar{u}_i'^2 \rangle \approx \langle u_i'^2 \rangle$, then

$$\frac{\langle \bar{u}_i'^2 \rangle}{u_\tau^2} = B_i - A_i \log\left(\frac{x_2}{\delta}\right) - \Delta_k^2 \left\langle \left(\frac{\partial \bar{u}_i'}{\partial x_k} \right)^2 \right\rangle + \mathcal{O}(\Delta_1^4 + \Delta_2^4 + \Delta_3^4), \quad (25)$$

where $A_2 = 0$. Eq. (25) shows that the wall-parallel turbulence intensities of the filtered field are not constraint to follow (22), and the major contributor to the departure from the classic log-law is the correction term on the right-hand side of (25). The error is then given by

$$\mathcal{E}_f \sim \Delta_k^2 \left\langle \left(\frac{\partial \bar{u}_i'}{\partial x_k} \right)^2 \right\rangle, \quad (26)$$

that together with the estimations for G in section IV.1 yields

$$\mathcal{E}_f^s \sim \Delta^0, \quad \mathcal{E}_f^i \sim \Delta^{2/3}, \quad (27)$$

which predict a rather low convergence rate for the LES turbulence intensities.

A limitation of (27) is that it does not provide a clear insight into the explicit logarithmic dependence of $\langle u_1'^2 \rangle$ and $\langle u_3'^2 \rangle$ with x_2 . An alternative procedure to estimate \mathcal{E}_f is to connect (22) and (23) by the spectrum of the streamwise velocity,

$$\frac{\langle u_i'^2 \rangle}{u_\tau^2} = 2 \int_0^\infty E_{u_i}(k_p, x_2) dk_p, \quad (28)$$

where E_{u_i} is the two-dimensional spectrum for the i -th velocity component as a function of $k_p^2 = k_1^2 + k_3^2$, where k_1 and k_3 are the streamwise and spanwise wavenumbers, respectively. Similarly,

$$\frac{\langle \bar{u}_i'^2 \rangle}{u_\tau^2} = 2 \int_0^\infty \bar{E}_{u_i}(k_p, x_2) dk_p, \quad (29)$$

where $\bar{E}_{u_i}(k_p, x_2)$ should be interpreted as the energy spectra of the filtered velocity. We will focus on the streamwise velocity component, but the reasoning below is also applicable to the spanwise component. Moreover, to make the problem tractable, we adopt the model spectrum for E_{u_1} from Fig. 8(b). The four different piecewise domains of the model correspond to the large-scale, shear-dominated [38], inertial [59] and viscous regimes [78], respectively. Evaluation of (28) using the model from Fig. 8(b) results in

$$\frac{\langle u_1'^2 \rangle}{2u_\tau^2} \approx \text{constant} - A \log\left(\frac{x_2}{b}\right), \quad (30)$$

where the contributions from inertial and viscous regimes have been neglected. The result is consistent with the logarithmic functional dependence of the streamwise turbulence intensity from (22). Under the severe assumptions that the filtering operator resembles a sharp Fourier cut-off, and neglecting filtering in the wall-normal direction,

$$\frac{\langle \bar{u}_1'^2 \rangle}{u_\tau^2} = 2 \int_0^\infty \bar{E}_{u_1}(k_p, x_2) dk_p \approx 2 \int_0^{\pi/\Delta} E_{u_1}(k_p, x_2) dk_p. \quad (31)$$

The difference $\langle u_1'^2 \rangle - \langle \bar{u}_1'^2 \rangle$ definitory of error (21) is

$$\mathcal{E}_f \sim \int_0^\infty E_{u_1}(k_p, x_2) dk_p - \int_0^{\pi/\Delta} E_{u_1}(k_p, x_2) dk_p, \quad (32)$$

and after integration we obtain

$$\mathcal{E}_f^s \sim \log(\Delta/x_2), \quad \mathcal{E}_f^i \sim \Delta^{2/3}, \quad (33)$$

for the shear-dominated and inertial regimes, respectively. When the filter cut-off lies within the k_p^{-1} regime, (33) predicts a $\log(\Delta/x_2)$ correction to the Δ^0 -dependence estimated in (27), although both cases imply a slow convergence with Δ . Additionally, for Δ within the shear-dominated region,

$$\langle \bar{u}_1'^2 \rangle \approx \text{constant} + \mathcal{O}(\log(\Delta)), \quad (34)$$

independently of x_2 , and the LES streamwise and spanwise turbulence intensities will not reproduce the asymptotic logarithmic profile. For the inertial range, the prediction of (33) coincides with the one reported in (27). Moreover, integration of the model spectrum yields

$$\langle \bar{u}_1'^2 \rangle \approx \text{constant} - A \log(x_2) + \mathcal{O}(\Delta^{2/3}), \quad (35)$$

and LES is expected to capture the classic logarithmic behavior in x_2 with a correction of the order of $\Delta^{2/3}$.

V.3. Numerical assessment

We aim to quantify the exponents α_f and γ_f for

$$\mathcal{E}_f \sim \left(\frac{\Delta}{\delta} \right)^{\alpha_f} Re_\tau^{\gamma_f}, \quad (36)$$

from LES data and the range of grid resolutions of interest in the present work. The results reported in this section are strictly valid for LES with DSM. Nevertheless, similar conclusions are drawn for AMD and $x_2 > 0.3\delta$ where the turbulence intensities predicted by AMD and DSM are almost indistinguishable. The results are also compared with filtered DNS data (fDNS), but this is only done qualitatively. For that, we use a three-dimensional box-filter with filter size equal to the LES grid resolution in each direction. The choice of this particular filter shape and filter size definition is arbitrary, and it was argued before that no specific form can be established *a priori* for implicitly-filtered LES.

Figs. 9(a)–(c) show the turbulence intensities as a function of the wall-normal direction for DNS and LES at $Re_\tau \approx 2000$ and various grid resolutions. The main observation from Fig. 9(a) is that the LES turbulence intensities diverge from DNS as the grid is coarsen, and the shape of the $\langle \tilde{u}_i'^2 \rangle$ becomes distinctively different from $\langle u_i'^2 \rangle$. Moreover, the effect is more pronounced closer to the wall. Hence, the DNS logarithmic behavior is not captured by LES when $\Delta = \mathcal{O}(\delta)$, in agreement with the discussion in section V.2. The error between LES and DNS is quantified in Fig. 9(d) and compared with the predictions from (27). The results show that $\mathcal{E}_{f,1}$ converges as $\Delta^{0.4}$, whereas $\mathcal{E}_{f,2}$ and $\mathcal{E}_{f,3}$ are well represented by $\Delta^{0.8}$.

The effect of the Reynolds number is evaluated in Fig. 10, which also includes comparisons with fDNS. The grid resolution (or filter size) for the LES and fDNS cases is set to i2 from table II ($\Delta = 0.1\delta$), and Re_τ ranges from ≈ 950 to ≈ 4200 . The dependence of $\mathcal{E}_{f,i}$ with Re_τ is weak, and the error remains roughly constant for $Re_\tau > 950$, from where we conclude that $\gamma_f \approx 0$. Therefore, the empirically measured error for the LES turbulence intensities scales as

$$\mathcal{E}_{f,1} \sim \left(\frac{\Delta}{\delta} \right)^{0.4} Re_\tau^0, \quad \mathcal{E}_{f,2/3} \sim \left(\frac{\Delta}{\delta} \right)^{0.8} Re_\tau^0, \quad (37)$$

for $\Delta > 0.025\delta$. The results also corroborate that the correct representation of $\langle \tilde{u}_i'^2 \rangle$ is more demanding than the mean velocity profile, consistent with the analysis in section V.2.

Fig. 10(a) also shows that the LES turbulence intensities are well approximated by fDNS, especially for the highest Reynolds numbers and far from the wall. Taking into account the considerations regarding the arbitrariness of the filter and the discussion from section V.1, the results should be interpreted as an indication that for the typical values of ν_t provided by SGS models, the LES fluctuating velocities are comparable to filtered DNS values at a filter size close to Δ .

Similarly to the mean velocity profile, the error from (21) can be re-evaluated locally along different wall-normal bands as a mean to explore the relevant physical scale-length to refer Δ . We define the local error for the turbulent kinetic energy $K = (u_1'^2 + u_2'^2 + u_3'^2)/2$ (analogously for LES) as

$$\mathcal{E}_{K,l}(x_2) = \left[\frac{\int_{x_2+d}^{x_2+d} \left(\langle \tilde{K} \rangle - \langle K \rangle \right)^2 dx_2}{\int_{0.2\delta}^{\delta} \langle K \rangle^2 dx_2} \right]^{1/2}, \quad (38)$$

which is numerically computed as (19). Results from Fig. 11 show that $\mathcal{E}_{K,l} \sim (\Delta/L_s)^{2/3}$, and L_s stands again as a sensible measure of the size of the energy-containing eddies relevant for quantifying LES errors. The collapse obtained by scaling the grid resolution by L_ε , η and L_t is less satisfactory, and the last two are not shown.

For completeness, we also consider the Reynolds stress tensor interpretation of $\langle u_i' u_j' \rangle$,

$$R_{ij}^{\text{DNS}} = \langle u_i' u_j' \rangle = \langle u_i u_j \rangle - \langle u_i \rangle \langle u_j \rangle, \quad (39)$$

where the diagonal components of R_{ij}^{DNS} are the mean squared DNS velocity fluctuations. As argued in Carati et al. [68], assuming $\langle \bar{\phi} \rangle \approx \langle \phi \rangle$,

$$R_{ij}^{\text{DNS}} = \langle u_i u_j \rangle - \langle u_i \rangle \langle u_j \rangle \approx \langle \bar{u}_i \bar{u}_j \rangle - \langle \bar{u}_i \rangle \langle \bar{u}_j \rangle \approx \langle \tilde{u}_i \tilde{u}_j \rangle + \langle \tau_{ij}^{\text{SGS}} \rangle - \langle \tilde{u}_i \rangle \langle \tilde{u}_j \rangle = R_{ij}^{\text{LES}}. \quad (40)$$

Thus, the main difference between considering $\langle u_i' u_j' \rangle$ as a stress rather than a velocity variance lies on the contribution of the SGS tensor. An advantage of (40) is that R_{ij}^{DNS} and R_{ij}^{LES} are directly comparable without prescribing a

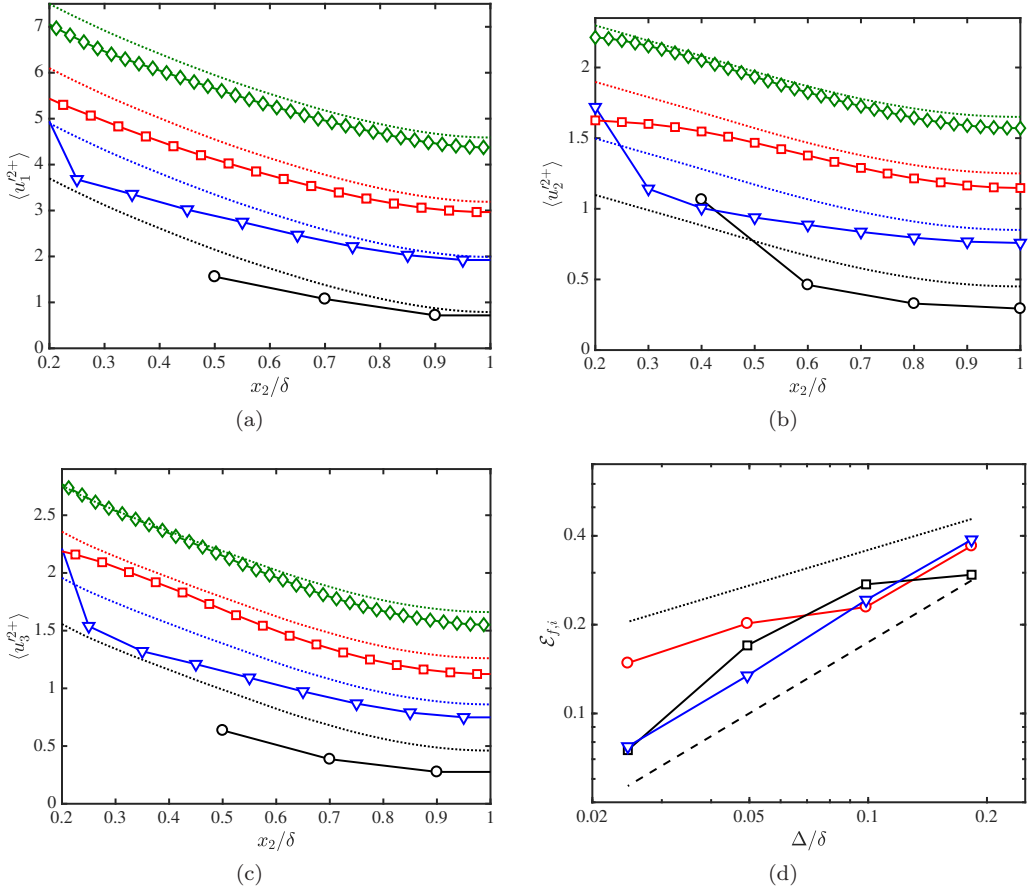


FIG. 9: Streamwise (a), wall-normal (b), and spanwise (c) turbulence intensities as a function of the wall-normal distance for different grid resolutions at $Re_\tau \approx 2000$. Symbols represent LES cases for different grid resolutions: circles, DSM2000-EWS-i1; triangles, DSM2000-EWS-i2; squares, DSM2000-EWS-i3; diamonds, DSM2000-EWS-i4. For clarity, cases DSM2000-EWS-i2, DSM2000-EWS-i3 and DSM2000-EWS-i4 are vertically shifted by 1.2, 2.4 and 3.8 wall units, respectively. The first two points closer to the wall for case DSM2000-EWS-i1 are omitted as they are contaminated by the nonphysical solution close to the wall. For comparison, each LES case is accompanied by DNS data (dotted lines) vertically shifted by the same amount. (d) Error in the turbulence intensities $\mathcal{E}_{f,i}$ as a function of the characteristic grid resolution. Symbols and colors are: red circles, $\mathcal{E}_{f,1}$; black squares, $\mathcal{E}_{f,2}$; blue triangles, $\mathcal{E}_{f,3}$. The dashed and dotted lines are $\mathcal{E}_f \sim \Delta^{0.8}$ and $\mathcal{E}_f \sim \Delta^{0.4}$, respectively.

particular filtering operation. However, the approach is also accompanied by a limitation for the incompressible Navier–Stokes equations where only the traceless part of τ_{ij}^{SGS} is modeled. Hence, in order to allow for straight comparisons only the deviatoric contributions of R_{ij}^{DNS} and R_{ij}^{LES} must be taken into consideration [79]. An error analogous to (21) can be defined using the traceless counterparts of R_{ij}^{DNS} and R_{ij}^{LES} . The results, omitted for brevity, show that the errors have a weak dependence on the grid resolution and follow $\sim (\Delta/\delta)^{\alpha_f}$, with $\alpha_f < 2/3$.

VI. ERROR SCALING OF THE VELOCITY SPECTRA

We consider the two-dimensional kinetic energy spectrum for the unfiltered velocity field at a given wall-normal distance x_2 , $E_K(k_1, k_3, x_2) = \langle \hat{u}_i \hat{u}_i^* \rangle_t / 2$, where $\langle \cdot \rangle$ is the Fourier transform in the homogeneous directions, $(\cdot)^*$ denotes complex conjugate, and $\langle \cdot \rangle_t$ is average in time. Similarly, the kinetic energy spectrum for the LES velocity is $\hat{E}_K(k_1, k_3, x_2) = \langle \hat{\tilde{u}}_i \hat{\tilde{u}}_i^* \rangle_t / 2$. The magnitude of E_K is given by

$$\langle u_1'^2 + u_2'^2 + u_3'^2 \rangle = 2 \int_0^\infty \int_0^\infty E_K(k_1, k_3, x_2) dk_1 dk_3, \quad (41)$$

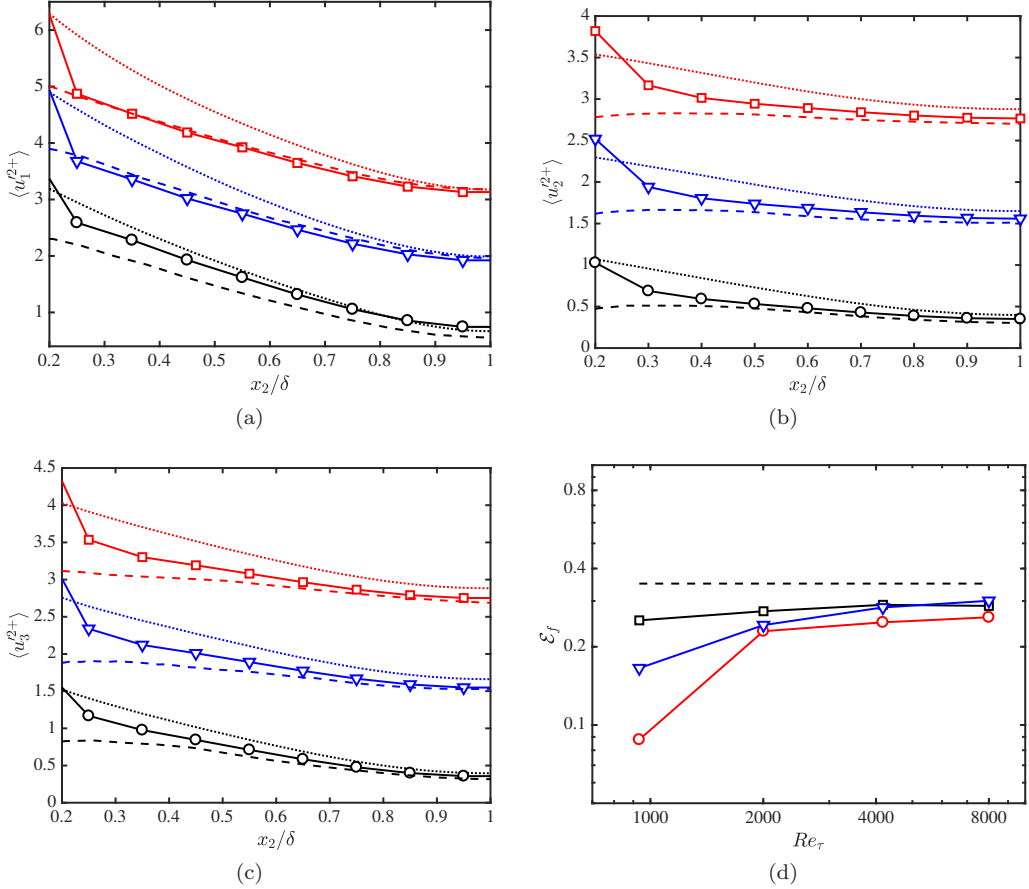


FIG. 10: Streamwise (a), wall-normal (b), and spanwise (c) turbulence intensities as a function of the wall-normal distance for different different Reynolds numbers with grid resolution $i2$. Symbols represent LES cases for different Reynolds numbers: circles, DSM950-EWS-i2; triangles, DSM2000-EWS-i2; squares, DSM4200-EWS-i2. For clarity, cases DSM2000-EWS-i2 and DSM4200-EWS-i2 are vertically shifted by 1.2 and 2.4 wall units, respectively. For comparison, each LES case is accompanied by DNS data (dotted lines) and box filtered DNS data (dashed lines) vertically shifted by the same amount. (d) Error in the turbulence intensities $\mathcal{E}_{f,i}$ as a function of the Reynolds number. Symbols and colors are: red circles, $\mathcal{E}_{f,1}$; black squares, $\mathcal{E}_{f,2}$; blue triangles, $\mathcal{E}_{f,3}$. The dashed line is $\mathcal{E}_f = 0.35$.

(analogously for \tilde{E}_K) and it was investigated in the previous section. We are now concerned with the distribution of energy in the homogeneous scale-space at a given wall-normal distance and define the error in the energy spectrum as

$$\mathcal{E}_s(x_2) = \left[\frac{\int_0^\infty \int_0^\infty (\tilde{E}_K - E_K)^2 dk_1 dk_3}{\int_0^\infty \int_0^\infty E_K^2 dk_1 dk_3} \right]^{1/2}. \quad (42)$$

VI.1. Theoretical estimations

The effect of τ_{ij} on the distribution of energy can be analyzed by considering the spectral kinetic energy equation for \tilde{E}_K at a given wall-normal distance,

$$\frac{\partial \tilde{E}_K}{\partial t} = \hat{P} + \hat{T} + \hat{\Pi} + \hat{D} + \hat{\varepsilon} + \hat{D}_\tau + \hat{\varepsilon}_\tau, \quad (43)$$

where the first five terms in the right-hand are the production rate of the turbulent kinetic energy (\hat{P}), turbulent transport (\hat{T}), pressure diffusion ($\hat{\Pi}$), viscous diffusion (\hat{D}), and the molecular dissipation rate ($\hat{\varepsilon}$), respectively. The

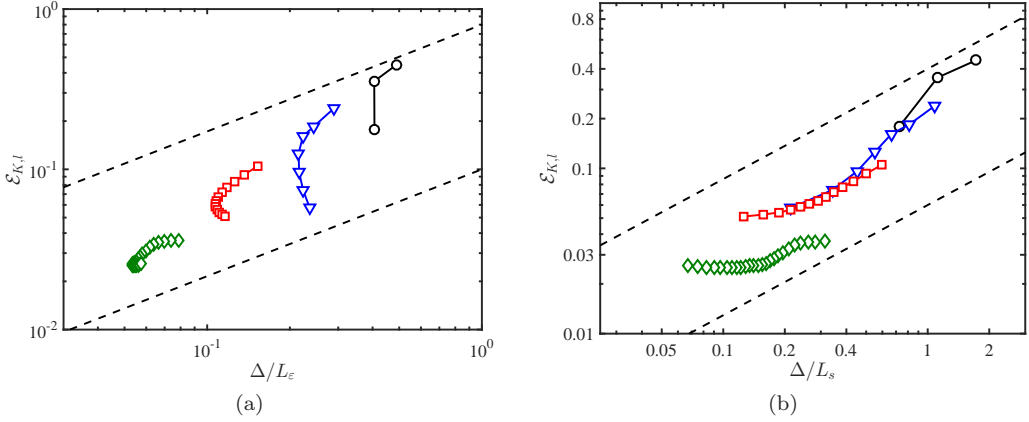


FIG. 11: Local error in the turbulence kinetic energy $\mathcal{E}_{K,l}(x_2)$ as a function of Δ normalized by (a) L_ε and (b) $L_s(x_2)$. Colors represent different grid resolutions from table II: black, i1; blue, i2; red, i3; green, i4. LES cases are DSM2000-EWS-i1, DSM2000-EWS-i2, DSM2000-EWS-i3 and DSM2000-EWS-i4. Dashed lines are (a) $\mathcal{E}_{K,l} = 0.1(\Delta/L_\varepsilon)^{2/3}$ and $\mathcal{E}_{K,l} = 0.8(\Delta/L_\varepsilon)^{2/3}$, (b) $\mathcal{E}_{K,l} = 0.06(\Delta/L_s)^{2/3}$ and $\mathcal{E}_{K,l} = 0.4(\Delta/L_s)^{2/3}$.

explicit form of these terms can be found in Mizuno [80]. We will focus on the contributions from τ_{ij} ,

$$\hat{\varepsilon}_\tau = \mathbb{R} \left[-\sqrt{-1}k_1 \langle \hat{u}_i^* \hat{\tau}_{i1} \rangle_t - \sqrt{-1}k_3 \langle \hat{u}_i^* \hat{\tau}_{i3} \rangle_t + \left\langle \frac{\partial \hat{u}_i^*}{\partial x_2} \hat{\tau}_{i2} \right\rangle_t \right], \quad \text{and} \quad \hat{D}_\tau = \mathbb{R} \left[-\frac{\partial \langle \hat{\tau}_{i2} \hat{u}_i^* \rangle_t}{\partial x_2} \right], \quad (44)$$

where \mathbb{R} denotes real part. The term $\hat{\varepsilon}_\tau$ is the dissipation rate of the spectral kinetic energy by τ_{ij} , while \hat{D}_τ is the wall-normal turbulent transport by τ_{ij} . A detailed equation for the spectral error can be derived from (43) although the result is quite cumbersome. Instead, we will assume by dimensional arguments that the functional dependence of \mathcal{E}_s on Δ is proportional to the temporal integration of $(\hat{\varepsilon}_\tau + \hat{D}_\tau)$,

$$\mathcal{E}_s \sim \int_0^{t_c} (\hat{\varepsilon}_\tau + \hat{D}_\tau) dt \sim \Delta^2 G, \quad (45)$$

where $t_c \sim G^{-1}$ is the characteristic time-scale, and the estimated errors scale as

$$\mathcal{E}_s^s \sim \Delta, \quad \mathcal{E}_s^i \sim \Delta^{4/3} \quad (46)$$

for grid resolutions comparable to eddies in the shear-dominated or inertial range, respectively.

VI.2. Energy-resolving grid resolution estimations

Previous to the numerical assessment of the error scaling, we estimate the required LES grid resolution to resolved 90% of the turbulent kinetic energy at a given wall-normal distance from the two-dimensional spectral energy density $E_K(\lambda_1, \lambda_3, x_2)$ as a function of the streamwise and spanwise wavelengths, namely $\lambda_1 = 2\pi/k_1$ and $\lambda_3 = 2\pi/k_3$, respectively. Simple models describing the 2-D spectral contributions for moderate and high Reynolds numbers have been proposed by Del Álamo et al. [81] and Chandran et al. [82], respectively. However, both works focus on the energy bounds for the large scales, whereas we are interested in the limiting length-scales for the smaller energy-containing eddies, that is, we are seeking for the minimum streamwise and spanwise grid spacing, Δ_1^{\min} and Δ_3^{\min} such that $E_K(\lambda_1 > 2\Delta_1^{\min}, \lambda_3 > 2\Delta_3^{\min}, x_2)$ contains 90% of the total turbulent kinetic energy. Fig. 12(a) shows contours of 90% energy for E_K at different wall-normal distances. As expected, the size of the energy-containing eddies shrinks as they get closer to the wall. As postulated by the attached eddy hypothesis [70], the only relevant length-scales for the motions spanning along the logarithmic layer is x_2 , which allows to write the energy spectra as

$$E_K = E_K(\lambda_1/x_2, \lambda_3/x_2). \quad (47)$$

The scaling from (47) has been extensively assessed in the literature [43, 45] and DNS results are plotted in Fig. 12(b) for various heights and Reynolds numbers. Eq. (47) enables the estimation of energy bounds that are approximately

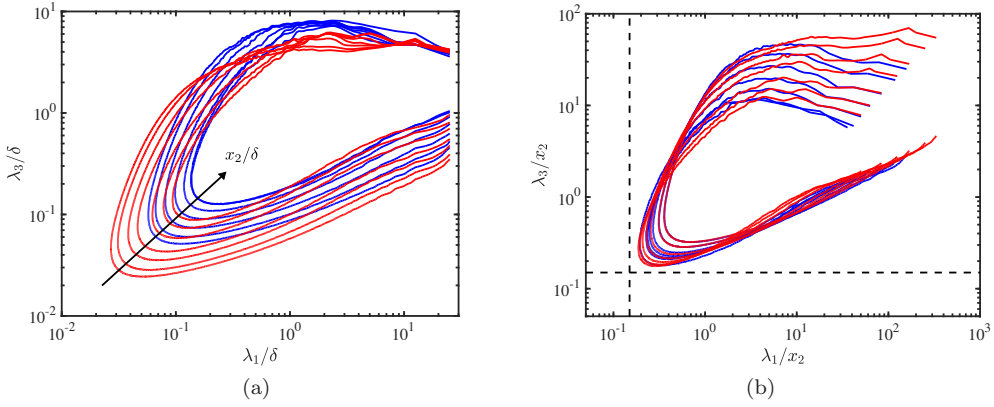


FIG. 12: Premultiplied two-dimensional kinetic energy spectra for DNS data as a function of the streamwise and spanwise wavelengths normalized by (a) δ , and (b) wall-normal distance. Colors are blue for $Re_\tau \approx 950$ and red for $Re_\tau \approx 2000$. Different contours denote different heights $x_2/\delta = 0.16, 0.21, 0.30, 0.40, 0.50$ and 0.60 for $Re_\tau \approx 950$, and $x_2/\delta = 0.08, 0.10, 0.15, 0.20, 0.30, 0.40$ and 0.50 for $Re_\tau \approx 2000$. Contours contain 90% of the turbulent kinetic energy.

valid at all the wall-normal distances within the outer layer. Taking $(\lambda_1)_{min} = 2\Delta_1^{min}$ and $(\lambda_3)_{min} = 2\Delta_3^{min}$, the *a priori* minimum wall-parallel grid resolutions to resolved 90% of the turbulent kinetic energy at x_2 are

$$\left(\frac{\lambda_1}{x_2}\right)_{min} = \frac{2\Delta_1^{min}}{x_2} \approx 0.15, \quad \left(\frac{\lambda_3}{x_2}\right)_{min} = \frac{2\Delta_3^{min}}{x_2} \approx 0.15. \quad (48)$$

For example, to resolved 90% of the turbulent kinetic energy at $x_2 \approx 0.5\delta$, we will require $\Delta_1 = \Delta_3 \approx 0.04\delta$. The grid resolution guidelines in (48) imply that $\Delta_1 \approx \Delta_3$, in contrast with the common choice of $\Delta_1 > \Delta_3$ among LES practitioners, and usually argued in terms of the elongated streamwise velocity streaks typical of wall-bounded flows. However, it was shown in Fig. 12(b) that, given its small-scale nature, the ‘nose’ of the spectra is roughly isotropic and located at $\lambda_1 \approx \lambda_3$, which justifies the choice of $\Delta_1 \approx \Delta_3$. Nevertheless, it would be reasonable to choose $\Delta_1 > \Delta_3$ for coarser grid resolutions aiming to resolve a lower fraction of the turbulent kinetic energy.

VI.3. Numerical assessment

Fig. 13 displays the premultiplied two-dimensional spectra of the streamwise velocity for fDNS and LES (with DSM, AMD, and no explicit SGS model). The filtered spectra was calculated from box-filtered DNS data with a filter size $\Delta_1 \times \Delta_2 \times \Delta_3$. The results show that both DSM and AMD perform similarly, and that the LES spectra is representative of the expected energy distribution for the filtered velocities (Figs. 13a-c), although the LES prediction tends to be biased towards smaller scales for all grid resolutions.

For cases without explicit SGS model, the spectra is completely misrepresented for $\Delta > 0.05\delta$ (Figs. 13d-e), with most of the energy piled up close to the smallest scales supported by the grid. The physical interpretation of this effect was provided in section V.1 in terms of the necessary velocity gradients to comply with the conservation of energy. Figs. 13(d)-(e) are just the spectral depiction of the same effect, i.e., the energy cascades towards the smallest available scales until the resulting gradients can balance the input power driving the channel. The distribution of energy changes drastically for $\Delta < 0.05\delta$, where large-scale streaks are now a clear constituent feature of the flow (Fig. 13f). The result is consistent with the visualizations in Fig. 5(d), which shows a clear streaky pattern in the streamwise velocity for $\Delta = 0.025\delta$, but a notably different non-streaky structure for $\Delta > 0.05\delta$. The existence of this critical grid resolution may be connected to the grid requirements estimated in section VI.2, where it was concluded that $\Delta \approx 0.04\delta$ in order to capture at least 90% of the turbulent kinetic energy at $x_2 \approx 0.5\delta$. This seems to be a necessary requirement to support the development of streaks in the absence of SGS model, at least for the particular numerical discretization adopted in this study.

Two mechanisms are potentially responsible for the improvements reported in Fig. 13 for cases with SGS model with respect those without: the dissipation of energy piled up at the smallest LES scales by $\hat{\epsilon}_{SGS}$, and the redistribution of energy in the wall-normal direction by \hat{D}_{SGS} . These are the LES counterparts of $\hat{\epsilon}_\tau$ and \hat{D}_τ discussed in section

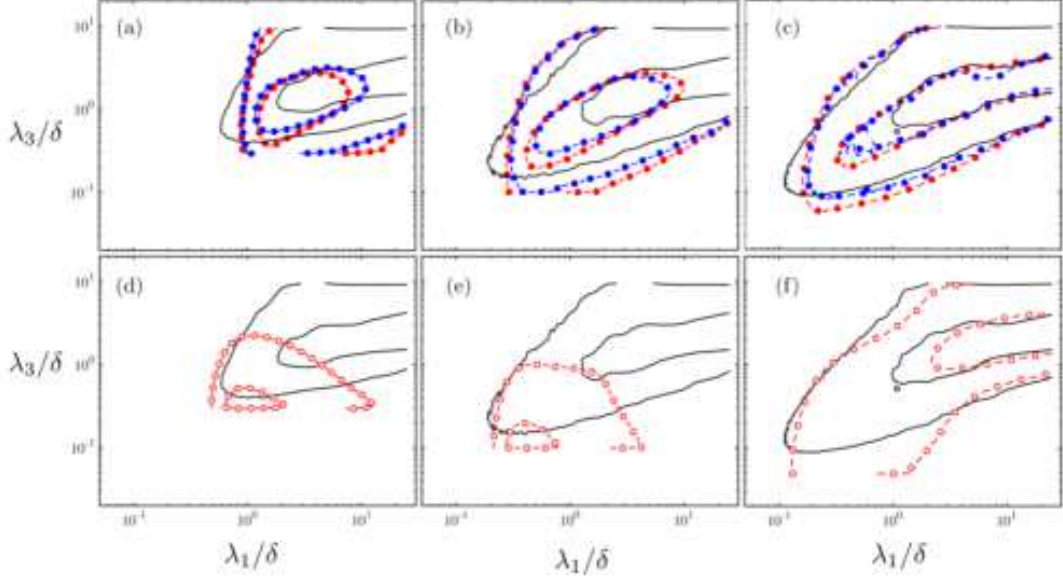


FIG. 13: Premultiplied two-dimensional streamwise velocity spectra as a function of the streamwise and spanwise wavelengths at $x_2 = 0.75\delta$ for different grid resolutions from table II. (a,d) i1 ($\Delta = 0.2\delta$), (b,e) i3 ($\Delta = 0.05\delta$), (c,f) i4 ($\Delta = 0.025\delta$). Colors and symbols are: red closed circles, DSM; blue closed circles, AMD; red open circles, no explicit SGS model. Solid lines represent box filtered DNS data. Contours are 0.1 and 0.6 of the maximum.

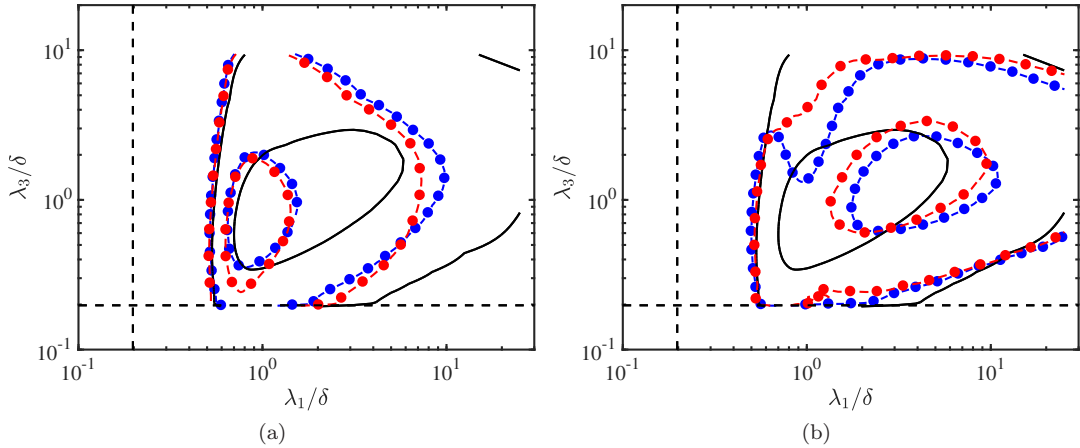


FIG. 14: Premultiplied two-dimensional spectra of the turbulent kinetic energy \tilde{E}_K (solid) compared with (a) the SGS dissipation rate of spectral kinetic energy $\hat{\varepsilon}_{SGS}$ and (b) the SGS turbulent transport \hat{D}_{SGS} (circles) as function of the streamwise and spanwise wavelengths at $x_2 = 0.75\delta$. Colors are: red, DSM2000-EWS-i2; blue, AMD2000-EWS-i2. Contours are 0.1 and 0.6 of the maximum of \tilde{E}_K and \hat{D}_{SGS} , and of the minimum of $\hat{\varepsilon}_{SGS}$. Dashed lines are $\lambda_1 = \lambda_3 = 0.20\delta$.

VI.1 and their spectra are plotted in Fig. 14. The computed values reveal that the main contributor is $\hat{\varepsilon}_{SGS}$ whose magnitude is roughly ten times larger than \hat{D}_{SGS} , and the improved predictions of the velocity spectra in Fig. 13(a) and (b) are mostly due to the removal of the excess of energy close to the grid cut-off.

Finally, the scaling of \mathcal{E}_s is evaluated in Fig. 15, which contains the errors for two wall-normal distances $x_2 = 0.2\delta$ and $x_2 = 0.75\delta$. The errors are well explained by Δ , as argued in VI.1 for grid resolutions within the shear-dominated range, and are insensitive to variations in the Reynolds number. In addition, \mathcal{E}_s increases when represented as a function of Δ/δ for different wall-normal heights due to the decrease of the energy-containing eddies relative to δ . Conversely, the errors collapse at different x_2 -locations for Δ/L_s , reinforcing L_s as the representative physical length-

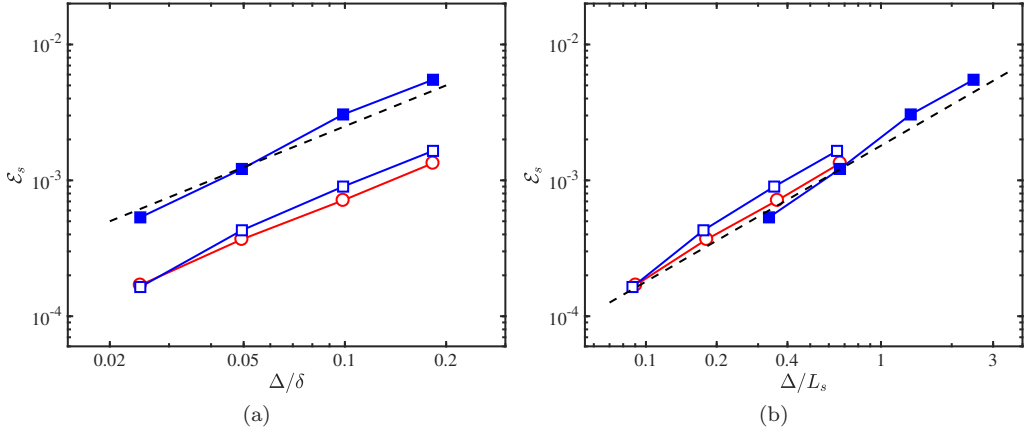


FIG. 15: Error in the kinetic energy spectra \mathcal{E}_s as a function of the characteristic grid size Δ scaled by (a) δ , and (b) $L_s(x_2)$. Open symbols are for $x_2 = 0.75\delta$, and closed symbols for $x_2 = 0.2\delta$. Colors are red for $Re_\tau \approx 950$ and blue for $Re_\tau \approx 2000$. Cases are for DSM but similar results are obtained for AMD. The dashed line is (a) $\mathcal{E}_s \sim \Delta/\delta$ and (b) $\mathcal{E}_s \sim \Delta/L_s$.

scale to measure the relative magnitude of Δ . In summary, we conclude that the errors in the kinetic energy spectra follow

$$\mathcal{E}_s \sim \left(\frac{\Delta}{L_s} \right) Re_\tau^0. \quad (49)$$

VII. CONCLUSIONS

Large-eddy simulation has emerged as a fundamental tool for both scientific research and industrial applications. However, the solutions provided by implicitly-filtered LES are grid-dependent, and multiple computations are required in order to attain meaningful conclusions. This brings the fundamental question of what is the expected LES error scaling as a function of Reynolds number and grid resolution, which has been the aim of the present investigation. In particular, we have focused on the outer layer of wall-bounded flows at high Reynolds numbers with grid resolutions comparable to the boundary layer thickness, as it is the typical scenario encountered in computational fluid mechanics for external aerodynamics.

LES of wall-bounded turbulence is, nevertheless, challenging since the energy-containing eddies are constrained to reduce their characteristic size in order to accommodate the presence of the wall. Proper wall-resolved LES calculations demand nested grid refinements to capture these eddies, with a high associated computational overhead. To make the problem tractable, previous studies have quantified SGS errors in WRLES at relatively low Reynolds numbers and unrealistically fine grids. In those conditions, most of the errors reported are probably dominated by the near wall-region, where SGS models are known to be deficient, while the outer layer resolution is fine enough for the contribution of the SGS models to be negligible. For example, we have shown that at $Re_\tau \approx 1000$ and 20 points per δ , the outer-layer mean velocity profile is well predicted by WMLES without any explicit SGS model due to the low Reynolds number. Since WMLES stands as the most feasible approach compared to WRLES or DNS, and given that in this cases the SGS model is only responsible for the outer flow, we have argued that it is necessary to consistently isolate the errors from those in the near-wall region.

In order to evaluate the performance of SGS models in the outer region independently of the effect of the wall, we have designed a numerical experiment referred to as exact-wall-stress channel flows where the integrated effect of the near-wall region on the outer flow is bypassed by supplying the exact mean stress at the wall. This numerical experiment retains the same physics as the traditional channel flow far from the wall, and hence is a suitable framework to test boundary layer flows. We have considered two SGS models, i.e., dynamic Smagorinsky model and minimum dissipation model, that are representative of eddy viscosity models with and without test filtering, respectively.

We have investigated the error scaling of the mean velocity profile, turbulence intensities, and kinetic energy spectra,

with the grid resolution and Reynolds number of the form

$$\mathcal{E}_q \sim \left(\frac{\Delta}{L} \right)^{\alpha_q} Re_{\tau}^{\gamma_q}, \quad (50)$$

where Δ and L are the characteristic grid size and the energy-containing eddies length-scale, respectively, and q denotes the quantity the error refers to, i.e. $q = m$ for the mean velocity profile, $q = f$ for the turbulence intensities, and $q = s$ for the kinetic energy spectra. Our results show that Δ/L is an intricate function of the flow state and grid resolution, but it is well approximated by the L_2 -norm of $(\Delta_1, \Delta_2, \Delta_3)$ divided by δ for quantities integrated over the outer layer, and by the shear length-scale, L_s , for local errors along the wall-normal direction. The observation that L_s is the relevant physical length-scale to refer Δ is consistent with its ability to represent the size of the energy-containing eddies. For $Re_{\tau} > 1000$, the errors are independent of the viscous effects and $\gamma \approx 0$, as expected for WMLES. We have derived the theoretical values for α_q by assuming an hypothetical SGS model that is able to represent the Reynolds stress tensor up to fourth order, and the results have been compared with the empirical values obtained by numerical simulations. To be consistent with the available computational resources, we have only considered cases where the grid resolutions are a fraction of the boundary layer thickness, and the corresponding LES filter cut-off lies either in the shear-dominated regime or in the inertial range, and always far from the viscous Kolmogorov region. Overall, the theoretical predictions match the numerical estimations, and we detail below the results of (50) for the different flow statistics investigated.

Errors in the mean velocity profile follow $\mathcal{E}_m \sim \epsilon \Delta / \delta$, where ϵ is a model dependent constant. Local measurements of the deviation of the LES profiles with respect to DNS have revealed that the errors increase with the proximity of the wall, and the prediction in the first off-wall grid point does not improve with grid refinement until the grid resolutions approach the WRLES regime.

We have reasoned that the turbulence intensities in implicitly-filtered LES are akin to those from filtered Navier-Stokes, but the former are controlled by the necessity of dissipating the energy input at the rate consistent with the statistically steady state, while the latter are directly linked to the filtering operation. In terms of convergence, the turbulence intensities are more demanding than the mean velocity profile and their error scales as $\mathcal{E}_f \sim (\Delta/\delta)^{\alpha_f}$ with $\alpha_f \approx 0.4 - 0.8$. Furthermore, in order to correctly capture the classic wall-normal logarithmic dependence of the streamwise and spanwise turbulence intensities, the grid resolution must lie within the inertial range, and we have shown that the turbulence intensities may exhibit a disparate behavior otherwise.

Errors in the relative distribution of the turbulent kinetic energy have been analyzed through the two-dimensional wall-parallel spectra, and they have been shown to follow $\mathcal{E}_s \sim (\Delta/L_s)$. We have pointed out that SGS models affect the distribution of energy via two difference mechanisms, namely, dissipation and wall-normal spatial transport, but that the former dominates being ten times larger in magnitude than the latter. The wall-parallel kinetic energy spectra from DNS was also utilized to estimate the LES grid requirements to resolved 90% of the turbulent kinetic energy as a function of x_2 , resulting in $\Delta_1 \approx \Delta_3 \approx 0.075x_2$. For example, if we wish to accurately resolved 90% of the turbulent kinetic energy at $x_2 \approx 0.5\delta$, then $\Delta_1 = \Delta_3 \approx 0.04\delta$. If we further assume an isotropic grid, the count results in ~ 25 points per boundary layer thickness.

In light of the present results, future efforts should be devoted in two directions. Firstly, enhanced SGS models may be desired to accelerate the convergence of the turbulence intensities in those cases where their accurate prediction is of great importance. Examples are noise signature prediction, or particle laden flows at certain Stokes numbers. Secondly, since our work relies on a wall model providing the exact mean stress at the wall, we have to emphasize the importance of developing and assessing the accuracy of wall models as a pacing item to achieve practical LES.

ACKNOWLEDGMENTS

This work was supported by NASA under the Transformative Aeronautics Concepts Program, grant no. NNX15AU93A. The authors would like to thank Dr. Perry Johnson and Maxime Bassenne for their insightful comments.

APPENDIX A. ERROR IN THE MEAN VELOCITY PROFILE FOR VREMAN MODEL, FINER GRIDS, AND WMLES

Cases with the Vreman model (VRM) are computed using the same numerical set-up described in section III.2 with a Vreman constant equal to 0.1, $Re_{\tau} \approx 4200$, and grid resolutions i1, i2 and i3. We will use the same nomenclature as in section III.2. The error in the mean velocity profile is shown in Fig. 16(a) and follows $\mathcal{E}_m \sim \Delta/\delta$ with values comparable to those obtained for AMD.

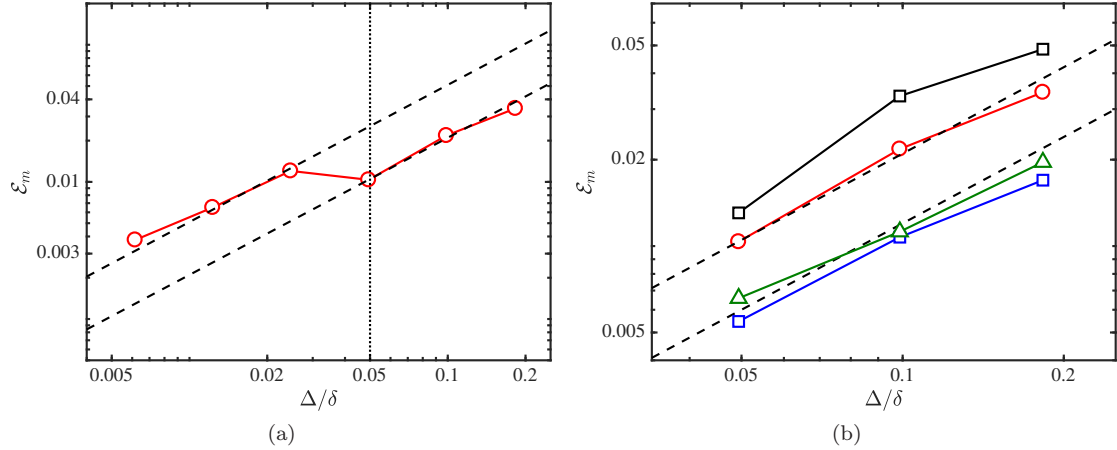


FIG. 16: Error in the mean velocity profile as a function of the characteristic grid resolution $\Delta = \sqrt{(\Delta_1^2 + \Delta_2^2 + \Delta_3^2)/3}$. (a) Assessment of finer grid resolutions for DSM4200-EWS-i1,i2,i3,i4,i5,i6. (b) Assessment of Vreman model and equilibrium wall model by Kawai and Larsson [32]. Colors and symbols are: red circles, DSM4200-EWS-i1,i2,i3; blue squares, AMD4200-EWS-i1,i2,i3; green triangles, VRM4200-EWS-i1,i2,i3; black squares, DSM4200-EQWM-i1,i2,i3. Dashed lines are $\mathcal{E}_m \sim \Delta/\delta$, and dotted line $\Delta = 0.05\delta$.

To test the effect of further grid refinements, two additional cases are computed with isotropic grids equal to $\Delta = 0.0125\delta$ (denoted by i5) and $\Delta = 0.0063\delta$ (i6) for DSM at $Re_\tau \approx 4200$. In order to alleviate the computational cost, the streamwise and spanwise channel lengths are reduced to $2\pi\delta$ and $\pi\delta$, respectively. The error in the mean velocity profile is plotted Fig. 16(a) which shows that $\mathcal{E}_m \sim \Delta/\delta$ is recovered below $\Delta \approx 0.05\delta$.

Finally, we also include results where the EWS condition from section III.1 is replaced by an actual wall model, namely, the equilibrium wall model by Kawai and Larsson [32] (EQWM). Cases are computed at $Re_\tau \approx 4200$ for DSM and grid resolutions i1, i2 and i3. The linear scaling observed for cases with EWS deteriorates slightly when the wall model is introduced, but remains close to $\mathcal{E}_m \sim \Delta/\delta$ as shown in Fig. 16(b).

[1] J. Slotnick, A. Khodadoust, J. Alonso, D. Darmofal, W. Gropp, E. Lurie, D. Mavriplis, CFD Vision 2030 Study: A Path to Revolutionary Computational Aerosciences, Tech. Rep. CR-2014-218178, NASA, 2014.

[2] S. B. Pope, Ten questions concerning the large-eddy simulation of turbulent flows, *New Journal of Physics* 6 (2004) 35.

[3] A. Leonard, Energy cascade in large-eddy simulations of turbulent fluid flows, in: F. Frenkiel, R. Munn (Eds.), *Turbulent Diffusion in Environmental Pollution*, volume 18 of *Advances in Geophysics*, Elsevier, 1975, pp. 237 – 248.

[4] R. A. Clark, J. H. Ferziger, W. C. Reynolds, Evaluation of subgrid-scale models using an accurately simulated turbulent flow, *J. Fluid Mech.* 91 (1979) 1–16.

[5] O. Métais, M. Lesieur, Spectral large-eddy simulation of isotropic and stably stratified turbulence, *Journal of Fluid Mechanics* 239 (1992) 157–194.

[6] H. Kobayashi, Y. Shimomura, The performance of dynamic subgrid-scale models in the large eddy simulation of rotating homogeneous turbulence, *Phys. Fluids* 13 (2001) 2350–2360.

[7] B. Vreman, B. Geurts, H. Kuerten, Large-eddy simulation of the temporal mixing layer using the clark model, *Theoretical and Computational Fluid Dynamics* 8 (1996) 309–324.

[8] B. Vreman, B. Geurts, H. Kuerten, Large-eddy simulation of the turbulent mixing layer, *Journal of Fluid Mechanics* 339 (1997) 357–390.

[9] U. Piomelli, P. Moin, J. H. Ferziger, Model consistency in large eddy simulation of turbulent channel flows, *The Physics of fluids* 31 (1988) 1884–1891.

[10] M. Germano, U. Piomelli, P. Moin, W. H. Cabot, A dynamic subgrid-scale eddy viscosity model, *Phys. Fluids A* 3 (1991) 1760.

[11] D. Chung, B. McKeon, Large-eddy simulation of large-scale structures in long channel flow, *Journal of Fluid Mechanics* 661 (2010) 341–364.

[12] J. Bonnet, R. Moser, W. Rodi, A selection of test cases for the validation of large eddy simulations of turbulent flows, AGARD advisory report 345 (1998) 1–35.

[13] J. Meyers, B. J. Geurts, M. Baelmans, Database analysis of errors in large-eddy simulation, *Phys. Fluids* 15 (2003) 2740–2755.

[14] J. Meyers, B. Geurts, P. Sagaut, A computational error-assessment of central finite-volume discretizations in large-eddy

simulation using a smagorinsky model, *Journal of Computational Physics* 227 (2007) 156 – 173.

[15] J. Meyers, Error-landscape assessment of large-eddy simulations: A review of the methodology, *Journal of Scientific Computing* 49 (2011) 65–77.

[16] J. Meyers, P. Sagaut, Is plane-channel flow a friendly case for the testing of large-eddy simulation subgrid-scale models?, *Phys. Fluids* 19 (2007) 048105.

[17] P. P. Sullivan, E. G. Patton, The effect of mesh resolution on convective boundary layer statistics and structures generated by large-eddy simulation, *Journal of the Atmospheric Sciences* 68 (2011) 2395–2415.

[18] R. J. A. M. Stevens, M. Wilczek, C. Meneveau, Large-eddy simulation study of the logarithmic law for second- and higher-order moments in turbulent wall-bounded flow, *J. Fluid Mech.* 757 (2014) 888–907.

[19] H. B. Toda, O. Cabrit, K. Truffin, G. Bruneaux, F. Nicoud, Assessment of subgrid-scale models with a large-eddy simulation-dedicated experimental database: The pulsatile impinging jet in turbulent cross-flow, *Phys. Fluids* 26 (2014) 075108.

[20] O. Lehmkuhl, G. Park, P. Moin, LES of flow over the NASA Common ResearchModel with near-wall modeling, *Center for Turbulence Research - Proceedings of the Summer Program* (2016) 335–341.

[21] B. J. Geurts, J. Fröhlich, A framework for predicting accuracy limitations in large-eddy simulation, *Physics of Fluids* 14 (2002) L41–L44.

[22] M. Klein, An attempt to assess the quality of large eddy simulations in the context of implicit filtering, *Flow, Turbulence and Combustion* 75 (2005) 131–147.

[23] M. Freitag, M. Klein, An improved method to assess the quality of large eddy simulations in the context of implicit filtering, *Journal of Turbulence* 7 (2006) N40.

[24] I. Celik, M. Klein, J. Janicka, Assessment measures for engineering les applications, *Journal of Fluids Engineering* 131 (2009) 031102–031102–10.

[25] G. Nastac, J. W. Labahn, L. Magri, M. Ihme, Lyapunov exponent as a metric for assessing the dynamic content and predictability of large-eddy simulations, *Phys. Rev. Fluids* 2 (2017) 094606.

[26] D. R. Chapman, Computational aerodynamics development and outlook, *AIAA J.* 17 (1979) 1293–1313.

[27] H. Choi, P. Moin, Grid-point requirements for large eddy simulation: Chapman’s estimates revisited, *Phys. Fluids* 24 (2012) 011702.

[28] J. Jiménez, Cascades in wall-bounded turbulence, *Annual Review of Fluid Mechanics* 44 (2012).

[29] J. Larsson, S. Kawai, J. Bodart, I. Bermejo-Moreno, Large eddy simulation with modeled wall-stress: recent progress and future directions, *Mechanical Engineering Reviews* 3 (2016) 15–00418.

[30] P. P. Sullivan, J. C. McWilliams, C.-H. Moeng, A grid nesting method for large-eddy simulation of planetary boundary-layer flows, *Boundary-Layer Meteorology* 80 (1996) 167–202.

[31] J. Jiménez, R. D. Moser, Large-eddy simulations: Where are we and what can we expect?, *AIAA J.* 38 (2000) 605–612.

[32] S. Kawai, J. Larsson, Wall-modeling in large eddy simulation: Length scales, grid resolution, and accuracy, *Physics of Fluids* 24 (2012) 015105.

[33] S. Chen, Z. Xia, S. Pei, J. Wang, Y. Yang, Z. Xiao, Y. Shi, Reynolds-stress-constrained large-eddy simulation of wall-bounded turbulent flows, *J. Fluid Mech.* 703 (2012) 1–28.

[34] A. Rouhi, U. Piomelli, B. J. Geurts, Dynamic subfilter-scale stress model for large-eddy simulations, *Phys. Rev. Fluids* 1 (2016) 044401.

[35] A. Rasam, G. Brethouwer, P. Schlatter, Q. Li, A. V. Johansson, Effects of modelling, resolution and anisotropy of subgrid-scales on large eddy simulations of channel flow, *J. Turbul.* 12 (2011) 1–20.

[36] J. Lee, M. Cho, H. Choi, Large eddy simulations of turbulent channel and boundary layer flows at high reynolds number with mean wall shear stress boundary condition, *Physics of Fluids* 25 (2013) 110808.

[37] S. B. Pope, *Turbulent Flows*, Cambridge University Press, 2000.

[38] A. E. Perry, C. J. Abell, Asymptotic similarity of turbulence structures in smooth- and rough-walled pipes, *J. Fluid Mech.* 79 (1977) 785 – 799.

[39] J. Jiménez, Turbulent flows over rough walls, *Ann. Rev. Fluid Mech.* 36 (2004) 173–196.

[40] O. M. Bakken, P. Å. Krogstad, A. Ashrafiyan, H. I. Andersson, Reynolds number effects in the outer layer of the turbulent flow in a channel with rough walls, *Phys. Fluids* 17 (2005) 065101.

[41] O. Flores, J. Jiménez, Effect of wall-boundary disturbances on turbulent channel flows, *J. Fluid Mech.* 566 (2006) 357–376.

[42] O. Flores, J. Jiménez, J. C. del Álamo, Vorticity organization in the outer layer of turbulent channels with disturbed walls, *J. Fluid Mech.* 591 (2007) 145–154.

[43] Y. Mizuno, J. Jiménez, Wall turbulence without walls, *J. Fluid Mech.* 723 (2013) 429–455.

[44] D. Chung, J. P. Monty, A. Ooi, An idealised assessment of townsend’s outer-layer similarity hypothesis for wall turbulence, *J. Fluid Mech.* 742 (2014).

[45] A. Lozano-Durán, H. Bae, The role of the wall and the mean momentum transfer in wall-bounded turbulence, *J. Fluid Mech.* submitted (2018).

[46] P. Orlandi, *Fluid Flow Phenomena: A Numerical Toolkit*, number 1 in *Fluid Flow Phenomena: A Numerical Toolkit*, Springer, 2000.

[47] J. Kim, P. Moin, Application of a fractional-step method to incompressible Navier-Stokes equations, *J. Comp. Phys.* 59 (1985) 308–323.

[48] A. A. Wray, Minimal-storage time advancement schemes for spectral methods, Technical Report, NASA Ames Research Center, 1990.

[49] A. Lozano-Durán, H. J. Bae, Turbulent channel with slip boundaries as a benchmark for subgrid-scale models in LES, *Center for Turbulence Research - Annual Research Briefs* (2016) 97–103.

[50] H. J. Bae, A. Lozano-Durán, S. T. Bose, P. Moin, Turbulence intensities in large-eddy simulation of wall-bounded flows, *Phys. Rev. Fluids* 3 (2018) 014610.

[51] A. Lozano-Durán, M. J. P. Hack, P. Moin, Modeling boundary-layer transition in direct and large-eddy simulations using parabolized stability equations, *Phys. Rev. Fluids* 3 (2018) 023901.

[52] D. K. Lilly, A proposed modification of the Germano subgrid-scale closure method, *Phys. Fluids A* 4 (1992) 633–635.

[53] W. Rozema, H. J. Bae, P. Moin, R. Verstappen, Minimum-dissipation models for large-eddy simulation, *Phys. Fluids* 27 (2015) 085107.

[54] A. W. Vreman, An eddy-viscosity subgrid-scale model for turbulent shear flow: Algebraic theory and applications, *Phys. Fluids* 16 (2004) 3670–3681.

[55] S. Hoyas, J. Jiménez, Scaling of the velocity fluctuations in turbulent channels up to $Re_\tau=2003$, *Phys. Fluids* 18 (2006) 011702.

[56] A. Lozano-Durán, J. Jiménez, Effect of the computational domain on direct simulations of turbulent channels up to $Re_\tau = 4200$, *Phys. Fluids* 26 (2014) 011702.

[57] Y. Yamamoto, Y. Tsuji, Numerical evidence of logarithmic regions in channel flow at $Re_\tau = 8000$, *Phys. Rev. Fluids* 3 (2018) 012602.

[58] G. S. Winckelmans, A. A. Wray, O. V. Vasilyev, H. Jeanmart, Explicit-filtering large-eddy simulation using the tensor-diffusivity model supplemented by a dynamic smagorinsky term, *Phys. Fluids* 13 (2001) 1385–1403.

[59] A. N. Kolmogorov, The Local Structure of Turbulence in Incompressible Viscous Fluid for Very Large Reynolds' Numbers, in: *Dokl. Akad. Nauk SSSR*, volume 30, 1941, pp. 301–305.

[60] J. Deardorff, A numerical study of three-dimensional turbulent channel flow at large Reynolds numbers, *J. Fluid Mech.* 41 (1970) 453–480.

[61] A. Scotti, C. Meneveau, D. K. Lilly, Generalized smagorinsky model for anisotropic grids, *Phys. Fluids* 5 (1993) 2306–2308.

[62] P. R. Spalart, W. H. Jou, M. Strelets, S. R. Allmaras, et al., Comments on the feasibility of LES for wings, and on a hybrid RANS/LES approach, *Advances in DNS/LES* 1 (1997) 4–8.

[63] F. X. Trias, A. Gorobets, M. H. Silvis, R. W. C. P. Verstappen, A. Oliva, A new subgrid characteristic length for turbulence simulations on anisotropic grids, *Physics of Fluids* 29 (2017) 115109.

[64] H. Tennekes, H. Tennekes, J. Lumley, *A First Course in Turbulence*, MIT Press, 1972.

[65] Y. Mizuno, J. Jiménez, Mean velocity and length-scales in the overlap region of wall-bounded turbulent flows, *Phys. Fluids* 23 (2011) 085112.

[66] J. Larsson, S. Kawai, J. Bodart, I. Bermejo-Moreno, Large eddy simulation with modeled wall-stress: recent progress and future directions, *Mech. Eng. Rev.* 3 (2016) 1–23.

[67] T. S. Lund, The use of explicit filters in large eddy simulation, *Comput. Math. App.* 46 (2003) 603–616.

[68] D. Carati, G. S. Winckelmans, H. Jeanmart, On the modelling of the subgrid-scale and filtered-scale stress tensors in large-eddy simulation, *J. Fluid Mech.* 441 (2001) 119–138.

[69] H. J. Bae, A. Lozano-Durán, Towards exact subgrid-scale models for explicitly filtered large-eddy simulation of wall-bounded flows, *Center for Turbulence Research - Annual Research Briefs* (2017) 207–214.

[70] A. A. Townsend, *The structure of turbulent shear flow*, Cambridge Univ Press, 1976.

[71] I. Marusic, J. P. Monty, M. Hultmark, A. J. Smits, On the logarithmic region in wall turbulence, *J. Fluid Mech.* 716 (2013) R3.

[72] M. Hultmark, M. Vallikivi, S. C. C. Bailey, A. J. Smits, Turbulent pipe flow at extreme reynolds numbers, *Phys. Rev. Lett.* 108 (2012) 094501.

[73] J. Jiménez, S. Hoyas, Turbulent fluctuations above the buffer layer of wall-bounded flows, *J. Fluid Mech.* 611 (2008) 215–236.

[74] J. A. Sillero, J. Jiménez, R. D. Moser, One-point statistics for turbulent wall-bounded flows at reynolds numbers up to $\delta^+ \approx 2000$, *Phys. Fluids* 25 (2013) 105102.

[75] A. Lozano-Durán, J. Jiménez, Effect of the computational domain on direct simulations of turbulent channels up to $Re_\tau = 4200$, *Phys. Fluids* 26 (2014) 011702.

[76] M. Lee, R. D. Moser, Direct numerical simulation of turbulent channel flow up to $Re_\tau \approx 5200$, *Journal of Fluid Mechanics* 774 (2015) 395–415.

[77] W. K. Yeo, K. W. Bedford, Closure-free turbulence modeling based upon a conjuctive higher order averaging procedure, *Computational Methods in Flow Analysis* (1988) 844–851.

[78] R. H. Kraichnan, The structure of isotropic turbulence at very high reynolds numbers, *J. Fluid Mech.* 5 (1959) 497–543.

[79] G. Winckelmans, H. Jeanmart, D. Carati, On the comparison of turbulence intensities from large-eddy simulation with those from experiment or direct numerical simulation, *Physics of Fluids* 14 (2002) 1809–1811.

[80] Y. Mizuno, Spectra of energy transport in turbulent channel flows for moderate reynolds numbers, *J. Fluid Mech.* 805 (2016) 171–187.

[81] J. C. Del Álamo, J. Jiménez, P. Zandonade, R. D. Moser, Scaling of the energy spectra of turbulent channels, *J. Fluid Mech.* 500 (2004) 135–144.

[82] D. Chandran, R. Baidya, J. P. Monty, I. Marusic, Two-dimensional energy spectra in high-reynolds-number turbulent boundary layers, *J. Fluid Mech.* 826 (2017) R1.